INTRAVASCULAR OPTICAL COHERENCE TOMOGRAPHY IMAGE ANALYSIS

by

ZHAO WANG

Submitted in partial fulfillment of the requirements

For the degree of Doctor of Philosophy

Dissertation Adviser: Dr. Andrew M. Rollins

Department of Biomedical Engineering

CASE WESTERN RESERVE UNIVERSITY

May, 2013
CASE WESTERN RESERVE UNIVERSITY

SCHOOL OF GRADUATE STUDIES

We hereby approve the thesis/dissertation of

 Zhao Wang candidate for the Doctoral of Philosophy degree*.

(signed) Dr. Andrew M. Rollins   Dr. David L. Wilson   Dr.

Marco A. Costa   Dr. Guoqiang (GQ) Zhang   (date) Feb 28,

2013

*We also certify that written approval has been obtained for any

proprietary material contained therein.

Contents

1

2

3
List of Tables

4
List of Figures

Figure 1.6 (Page 34): Overview of the automated image processing methods developed in this thesis.

Figure 2.1 (Page 41): Efficient segmentation of the optimal 3-D lumen boundaries using a multi-resolution approach. A coarse level IVOCT pullback was generated by downsampling the original high resolution pullback in the axial and lateral dimensions. Graph cut was performed to extract the optimal lumen boundaries on the coarse level, which was then mapped back to the fine level. A second round graph cut was performed on the fine level, but is restricted to the narrow band voxels sounding the mapped surface (yellow dotted lines). Using this two-step approach, the computation time can be reduced from tens of hours down to seconds.

Figure 2.2 (Page 42): Segmentation of guide wires using the en face projection view. (a) An cross-section image of a pullback showing the guide wire region with a long dark shadow. (b) The en face projection view showing the guide wire region as a continuous dark band traversing the whole pullback. The white dotted line illustrates the position of the frame (a) in the pullback. The guide wire positions of all frames can be simultaneously found by segmenting the two boundaries of the dark band.

Figure 2.3 (Page 43): Under-adjustment (left) and over-adjustment (right) of z-offset in IVOCT images. Top: Cartesian coordinate; Bottom: corresponding polar coordinate.

Figure 2.4 (Page 45): Left: Automated IVOCT calibration as detecting two coupled boundaries of the plastic sheath outside the imaging probe. Right: Graph construction with inter-surface edges to constraint the two surfaces neither too close nor too far apart. The red dotted curve represent potential feasible surfaces.

Figure 2.5 (Page 48): Comparison of the accuracy of the selected frame for assessing MLA between the algorithm and two experienced IVOCT analysts. Left: the selected frame difference against gold standard of the algorithm and two analysts in the 62

pullbacks. Right: The percentage of selected frames with no difference, 1-5 frame difference (≤ 1mm) and >5 frame difference (> 1mm) difference against gold standard.

Figure 2.6 (Page 48): Bland-Altman plot of the MLA, minimum, mean and maximum lumen diameters determined by the algorithm and the two analysts, with reference to the gold standard.

Figure 2.7 (Page 50): Comparison between commercial software and the proposed method in automated lumen segmentation.

Figure 2.8 (Page 50): Examples of the automated lumen segmentation. (a) Large vessel. (b) Post-stenting case with thin neointima coverage. (c) Severe stenosis with the guide wire touching the lumen boundary. (d) Luminal protrusion artifacts.

Figure 2.9 (Page 51): With the lumen boundaries automatically segmented in all frames, the entire pullback can be 3-D rendered with a plot of the lumen area at each position side-by-side. In this example, the calculated MLA is in region B. In comparison, region A also has small lumen areas (but larger than MLA), and may be disregarded if only single frame numbers are observed. However, region A is proximal to region B, and might be hemodynamically more significant than region B (expected distal vessel tapering).

Figure 2.10 (Page 53): An example where the algorithm failed to correctly segment the lumen boundary at 9 o'clock (arrow).

Figure 3.1 (Page 61): Methodology for validation of fibrous cap luminal and abluminal boundary determination. The distance from the two boundaries to the lumen centroid was defined as and , respectively, and compared between the computer algorithm and human analysts. This distance was calculated along rays at intervals of one degree.

Figure 3.2 (Page 62): Manual measurements of the minimum cap thickness of the 14 lesions by the three analysts. (a): The difference of the selected frame for measuring the minimum cap thickness by the three analysts was plotted vs. the lesion number. The frame difference is against analyst 1. Frame difference of 0 indicates no difference. (b): The minimum cap thickness measured on the selected frame in (a). CCC: concordance correlation coefficient. CCC<0.4 is considered to be poor agreement. Dashed line: conventional cut-off value of 65μm for definition of TCFA. Under this definition, one of the three analysts held a different assessment of TCFA for 10 out of 14 lesions.

Figure 3.3 (Page 63): (a): Mean absolute difference (MAD) between automated and manual measurements by three observers. (b): Mean signed difference (MSD). Left: fibrous cap thickness determination. Middle: Luminal boundary determination. Right: Abluminal boundary determination. O: observer. Auto: computer algorithm.

Figure 3.4 (Page 64): In this case, the semi-automatically segmented fibrous cap boundary showed good agreement with all three human analysts.

Figure 3.5 (Page 64): In this case, the algorithm shows disagreement with the 3 analysts. The traced FC from analyst 2 is significantly thinner than that from the algorithm. In

6

comparison, the FC traced by analyst 3 around 9-10 o'clock is significantly thicker. Analyst 1 selected more circumferential distribution of FC for segmentation.

Figure 3.6 (Page 66): Two coronary arteries used in the validation study with fibrous caps (FC) rendered in a continuous color map indicating the thickness. Both of the two lesions contain TCFA (red arrows) and similar minimum cap thickness. However, the one shown in the lower panel contains a significantly larger surface area with thin cap as compared to the one in the upper panel.

Figure 3.7 (Page 69): In this case, the computer algorithm mistakenly identified luminal

blood as part of the tissue due to the contact between the blood and lumen boundary. In the blood-free region, the algorithm accurately segmented the boundary as compared to human analysts.

Figure 4.1 (Page 74): (a) The matched filter used for edge detection. (b) Binary edge detection result. (c) The initial contour generated from the binary edge image by morphological dilation.

Figure 4.2 (Page 76): Calcified plaque quantification metrics. The yellow dotted lines radiating from the centroid of the lumen serve as the direction along which the depth and thickness are measured. The red and blue double arrows indicate and for depth and thickness measurement, respectively. AFF is the largest angle between the rays across the CP boundaries.

Figure 4.3 (Page 78): Examples of calcified plaque segmentation results. (a–c) Original images. (d–f) Corresponding manual and automatic segmentation results. Red: observer 1; blue: observer 2; yellow: automatic method.

Figure 4.4 (Page 79): Left: Select slices from 40 slice segmentation. User provided input on slices 1, 10, 20, 33, and 40. Note incomplete contour in slice 24. Right: "Fast editing" is demonstrated. Incorrectly segmented slices are shown in the left pane. The user marks a small amount of input on only slice 27, and segmentation is recalculated in seconds, improving segmentation on neighboring slices as well.

Figure 5.1 (Page 82): Overview of the 3-D stent detection method.

Figure 5.2 (Page 85): The Bayesian network for inference of strut presence. (a) Top: Original OCT image in polar coordinate. Bottom: By calculating the mean intensity of the A-line within a fixed depth from the lumen boundary, the 2-D image is projected into a 1-D curve (plotted in an inverse scale). Searching for strut locations is equivalent to searching for peaks in the 1-D curve. (b) A Bayesian network representation based on principles of OCT image formation.

Figure 5.3 (Page 89): Individual frames in polar coordinates in the stented portion of the entire pullback were synthesized into an en face projection image.

Figure 5.4 (Page 91): (a) Representative image frame (Cartesian coordinate) from an OCT pullback showing a stent implanted in a coronary artery with new tissue growth. The distances from adjacent struts (blue dots) to the lumen centroid are kept within a

7

certain constraint. (b) Corresponding polar coordinate. (C) With the deformation constraint, the optimal depths (blue line) for all the struts form the global optimal surface in the graph constructed using only the pixels in the *strut lines*.

Figure 5.5 (Page 92): Illustration of stent area (the area enclosed by the stent struts), malapposition area (the area enclosed by the lumen boundary and malapposed struts) and neointima area (the area enclosed by the lumen boundary and tissue covered stent struts).

Figure 5.6 (Page 95): Human analyzed data used as the gold standard for validation. Manually marked strut are indicated by blue dots in the image. Only stent struts with bright bloom were analyzed by human analysts in order to minimize inter-observer varibility in strut-level analysis. For example, the yellow circled struts were not analyzed by human analysts. Inset: Human analysts marked the front edge, instead of the center of bloom for analysis.

Figure 5.7 (Page 98): Left: Bayesian classification affected by the training data size. The testing data are a subset of randomly selected 10 pullbacks (978 images) from the entire validation data set. Right: Performance of the stent strut detection in 8332 clinical images from 103 pullbacks. As the gold standard is "biased" that not every strut was analyzed manually (section III A), the actual precision of the method expected to be significantly underestimated. (a) and (b): Recall and precision for struts with different thickness of neointima coverage, respectively. These metrics are derived on a frame-by-frame basis. Tissue coverage was determined by the average thickness of all struts in a frame. (c) Overall performance using all the images. Here the metrics are derived on a pullback-by pullback basis.

Figure 5.8 (Page 99): Examples of automated stent strut detection in cases with stent implanted at different time points, images of varying quality and in the presence of various artifacts.

Figure 5.9 (Page 99): Examples of cases where the algorithm failed. (a) False positives were generated in shadow-like dark regions (yellow arrows). (b) Struts with very thick coverage and almost no shadows were not detected by the automated method (yellow arrows). (c): Near a stent strut branching (yellow arrow), the algorithm detected only one strut whereas there are actually two. A false positive is also detected by the algorithm (red arrow).

Figure 6.1 (Page 107): Intro-aortic OCT imaging of mouse aorta.

Figure 6.2 (Page 110): Macrophage accumulation detected by intra-aortic OCT and immunohistochemistry in ApoE-/- mouse. Representative intra-aortic OCT cross sectional images and corresponding (OCT), hematoxylin and eosin staining (HE), Mac-3 staining (Mac-3), and von kossa staining (Von Kossa) from 9-week ApoE-/- mouse on normal diet (control, upper row) and 29-week ApoE-/- mouse on high fat diet (bottom 3 rows) are shown. Accumulation of macrophages is shown as strong, bright back-scattered reflections. Please note the smooth circular contour in the upper row OCT image, corresponding to a normal wall morphology by histology.

Figure 6.3 (Page 110): Automatic segmentation results. Left: OCT image containing macrophages. Middle: Automatic segmented macrophages. Right Corresponding histology (Mac-3 stain).

9
Acknowledgements

I have been fortunate to work in an exciting area where I have the ability and enthusiasm to accomplish some meaningful work to potentially improve the diagnosis of heart diseases. This thesis would not have been possible without the support from many people.

To my advisor Dr. Andrew Rollins for guiding me through the thesis work and carefully revising my publications, while giving me enough freedom to explore my own ideas and interests. Also thank him for being a great advisor not only in academia, but also in personal lives.

To my collaborators and advisors Dr. David Wilson, Dr. Hiram Bezerra, Dr. Marco Costa and Dr. GQ Zhang, for providing me an excellent interdisciplinary team and numerous support, and making my project clinically relevant.

To all the members in Dr. Rollins' lab, Dr. Wilson's lab and the Cardiovascular Imaging Core Laboratory at the University Hospitals Case Medical Center, for many fruitful discussions and plenty of laughter. Special thanks to Dr. Michael Jenkins, who gave me many constructive ideas and helpful guidance on my research.

To my dear wife Xiaoyue Shi, who shared all the joy and tears with me throughout my thesis work, and is always supporting me to achieve my best.

To my parents who have always been standing behind me, and supporting me for any choice I made.

To all the friends I have made in Cleveland, for all the great times we have spent together.

List of Abbreviations

ApoE Apolipoprotein E

A-scan Axial Scan

BMS Bare-metal Stents

BVS Bioabsorbable Stents

CAD Coronary Artery Disease

CCC Concordance Correlation Coefficient

CHD Coronary Heart Disease

CP Calcified Plaques

DES Drug-eluting Stents

DP Dynamic Programming

DSC Dice's Coefficient

EEM External Elastic Membrane

FC Fibrous Caps

FDOCT Fourier Domain Optical Coherence Tomography

FN False Negatives

FP False Positive

GPU Graphical Processing Unit

IVOCT Intravascular Optical Coherence Tomography

IVUS Intravascular Ultrasound

MAD Mean Absolute Difference

MAP Maximum *a Posteriori*

MCD Mean Signed Difference

MCT Minimum Cap Thickness

MI Myocardial Infarction

MID Median Intensity Difference

MLA Minimal Luminal Area

MST Minimum Spanning Tree

NIH Neointima Hyperplasia

NSD Normalized Standard Deviation

OCT Optical Coherence Tomography

OFDI Optical Frequency Domain Imaging

OCTivat Intravascular OCT image Visualization and Analysis Toolkit

PCI Percutaneous Coronary Intervention

ROI Region of Interest

SC Shadow Contrast

STD Standard Deviation

SDF Signed Distance Function

SSOCT Swept-Source Optical Coherence Tomography

STEMI ST Segment Elevation Myocardial Infarction

TCFA Thin-cap Fibroatheroma

TN True Negatives

TP True Positives

Intravascular Optical Coherence Tomography Image Analysis

Abstract

By

ZHAO WANG

Coronary artery disease (CAD) is the leading cause of death in the world. Most acute coronary events such as heart attacks and sudden deaths are due to the rupture of atherosclerotic plaques inside the arteries. Intravascular Optical Coherence Tomography (IVOCT), a high resolution (10-20μm) imaging modality that performs cross-sectional imaging of coronary arteries by measuring echoes of backscattered light, is rapidly becoming a promising imaging modality for diagnosis of CAD. Compared to alternative technologies such as intravascular ultrasound (IVUS), IVOCT with better resolution allows characterization of atherosclerotic plaques and evaluation of coronary stenting with unprecendented details. Currently, analysis of OCT images has been typically conducted manually in an extremely time-consuming manner. The aim of this PhD dissertation is to develop advanced image processing algorithms and software to automate the task and thereby reduce the image analysis time drastically.

In this dissertation, we developed image analysis algorithms for a variety of IVOCT

applications, including: (1) 3-D lumen boundary segmentation, (2) Guide wire artifact segmentation, (3) Automated calibration of IVOCT images, (4) Volumetric quantification of fibrous caps, (5) Automated segmentation of calcified plaques, (6) Automated quantification of macrophages and (7) Automated stent analysis, covering almost all the

13

essential tasks performed in the Cardiovascular Imaging Core Laboratories (Core Lab). The algorithms we have developed have been extensively validated using a large number of data sets, and are robust to be used for real world clinical data analysis. Furthermore, we developed the prototype software OCTivat (intravascular OCT image visualization and analysis toolkit) for IVOCT image visualization and analysis, and it is being used by the interventional cardiologists in the Core Lab at the University Hospitals Case Medical Center. These image analysis methods, as well as OCTivat, can reduce the IVOCT image analysis time from tens of hours down to minutes. This may enable large clinical trial analysis and real-time feedback during clinical procedures, and may potentially improve patient care.

Chapter 1. Background

1.1 Coronary Artery Disease

Cardiovascular disease remains the No. 1 global cause of death, accounting for 17.3 million deaths per year, a number that is expected to grow to 23.6 million by 2030 (1). Each year, an estimate of 785,000 Americans will have a new coronary attack, and about 470,000 will have a recurrent event (2). Coronary artery disease (CAD) is caused by accumulation of fatty materials and build-up of atherosclerotic plaques inside the artery. As CAD proceeds, the coronary arteries may become narrower, with reduced blood flow to the heart. Eventually, the decreased blood flow may cause angina and other CAD

symptoms. Yet most of the acute coronary events are due to the rupture of vulnerable atherosclerotic plaques. When these plaques rupture, coronary thrombosis occurs, which is often life-threatening (3). Percutaneous coronary intervention (PCI) is the most common, and a well-established treatment modality for coronary artery disease, aiming at improving survival and relieving patient symptoms (4).

1.1.1 Atherosclerotic Plaques

There are three major types of atherosclerotic plaques associated with coronary artery diseases (CAD): lipid plaques, calcified plaques, and fibrous plaques.

Lipid plaques are rupture-prone plaques (5). Thin cap fibroatheroma (TCFA), often described as "vulnerable plaque", is an atherosclerotic plaque with a large lipid pool and a thin fibrous cap (<65μm) with infiltration of macrophages (3, 6-9). The rupture of TCFA is believed to cause most of the acute coronary events such as heart attacks and sudden deaths (9). Identifying these vulnerable plaques before symptoms arise, may

15

allow the adoption of preventive therapeutic measures to avoid subsequent myocardial infarctions and sudden deaths.

Calcified plaque is an important marker of atherosclerosis, and can provide an estimate of total coronary plaque burden for a patient (10-15). However, there is no clear relationship between calcification and plaque vulnerability (13). Calcified plaques are mechanically stiff. Superficial, heavily calcified lesions can result in under-expansion of coronary stents and often require usage of additional devices like rotational atherectomy (4, 16) before stenting.

Fibrous plaques contain solid fibrous or fibrocellular tissues and are clinically stable (5). They may evolve into vulnerable plaques by thinning fibrous caps overlying on a large lipid pool regulated by inflammation. Fibrous plaques are often involved in intima thickening, resulting in vessel stenosis and reduced blood flow.

Macrophages are associated with inflammation, and are often found in ruptured plaques (17). They can degrade the fibrous cap integrity, making it more prone to rupture (18). Macrophage is also a key mediator in both the early regulation and later more advanced plaque progression and rupture events (17, 18).

1.1.2 Coronary Stenting

Coronary stenting is the most common technique for coronary revascularization worldwide, and has been shown to improve survival rate in patients with significant luminal stenosis and acute syndromes such as STEMI (ST segment elevation myocardial infarction) (4). Improper deployment of stents and resulting tissue responses are associated with stent thrombosis, which is a life-threatening complication (19). Early

stents are mainly bare-metal stents (BMS) without a coating. The major limitation of BMS is that there is significant in-stent restenosis after stent implantation, and this may limit the long-term efficacy of coronary stenting (20). Drug-eluting stents (DES) is a later stent design with a special coating which releases drugs to prevent cell proliferation and neointima formation (21). DES can significantly reduce in-stent restenosis as compared to BMS (21, 22), and has been shown to have lower risk of major adverse cardiac events (21). However, DES is also associated with more incomplete neointima coverage 3-6

months after stent implantation, and therefore has higher risks of late stent thrombosis (23). More recently, stents made of bio-absorbable materials instead of metals have been developed (24, 25). They can be fully degraded by tissues ~2 years after stent implantation, and might have lower risks of late stent thrombosis because of no foreign materials left in the long run (24).

1.1.3 Imaging Technologies for Assessing CAD

Both non-invasive and invasive imaging technologies have been used to assess CAD, but at different levels. Commonly used non-invasive imaging modalities include CT and MRI, and their spatial resolution is limited to >1mm. Multislice Spiral Computed Tomography (MSCT)/Multidetector CT(MDCT) and Electron Beam CT (EBCT) are commonly used for evaluating general calcium score (10, 12, 14), which is an indicator for CAD. MRI can be used to evaluate acute myocardial ischemia and infarction (26), but its limited spatial resolution precludes its use for guiding PCI.

Invasive imaging modalities mainly include angiography, intravascular ultrasound (IVUS) and intravascular optical coherence tomography (IVOCT). Angiography is radiographic visualization of the coronary vessels after injecting a radio-opaque contrast

agent into the blood vessel and imaging using x-ray (27). The purpose of angiography is to define coronary anatomy and the degree of luminal obstruction of the coronary arteries. It is usually performed as part of cardiac catheterization and hemodynamic assessment as needed for a complete invasive diagnostic evaluation of the individual patient's cardiovascular condition (27). However, coronary angiography does not have sufficient resolution to assess individual plaque morphology and types, or to evaluate

coronary stenting.

IVUS and OCT are intravascular imaging technologies and they have been increasingly used in cardiac catheterization laboratories in order to provide safe, appropriate, and efficacious performance of PCI. Both IVUS and OCT use intravascular catheters for imaging and both can generate cross-sectional, volumetric images of coronary arteries by rotating and pulling back the catheter. IVUS utilizes ultrasound transducers to detect reflected ultrasound from the vessel and converts the signals into images (28). IVUS has a spatial resolution of 100-200µm, and can image deep tissues depending on the frequency of the ultrasound used (29). IVUS has the ability to assess the luminal boundaries, external elastic membrane (EEM), the leading edge of calcified plaques (high frequency ultrasound cannot penetrate calcified plaques, therefore cannot measure its thickness), and stenting. As ultrasound can penetrate blood, IVUS does not require blood clearing during imaging.

IVOCT (30-32) uses infrared light instead of ultrasound, and is based on interference of light. It has very high spatial resolution (10-20µm), more than 10 times higher than IVUS and other imaging modalities. The coherence gating of OCT also provides high contrast. Under IVOCT, a sharp delineation of the lumen contour allows for easy image

18

interpretation and provides the possibility for automated lumen area segmentation (30, 33). IVOCT can qualitatively characterize all major types of atherosclerotic plaques (34, 35). Moreover, it can quantitatively measure the fibrous cap thickness, assess superficial calcified plaques, and measure the tissue coverage of individual stent struts. IVOCT has also been suggested the ability to quantify macrophages (36). IVOCT has limited

penetration depth (1-2mm) and therefore does not have the ability to visualize deep EEM or to assess the total plaque burden (30). Additionally, IVOCT requires a blood-free environment for imaging and therefore temporary exclusion of blood using saline flushing or balloon occlusion is needed (36).

Table 1.1 below summarizes the invasive imaging technologies for quantitatively assessing atherosclerotic plaques and coronary stenting. Examples of each imaging technology are shown in Fig. 1.1. One can see that IVOCT has substantial advantages for assessment of superficial atherosclerotic plaques (34) and coronary stenting (37) over IVUS and Angiography. Moreover, the superior resolution and contrast of IVOCT provides the opportunity for automated image processing, which can drastically reduce the time needed for extracting the quantitative information for research and clinical purposes.

Angiography OCT IVUS

Figure 1.1. Example images from Angiography, OCT and IVUS (Images from Jang, I.-K. et al(35))

Table 1.1 Comparison between OCT, Angiography and IVUS

Quantitative Assessment	OCT	Angiography	IVUS
Lumen Area	+++	+	+++
Fibrous Caps	+++	N/A	N/A
Superficial Calcification	+++	N/A	+
Lipid plaques	++	NA	NA
Thrombus	+++	++	+
Stent Malapposition	+++	N/A	++/+
Strut Coverage	+++	N/A	+
Total Plaque Burden	N/A	N/A	+++

1.2 Optical Coherence Tomography (OCT)

OCT was invented by Huang et al at MIT in 1991(31). Since then, OCT has been quickly and successfully applied in ophthalmology (31, 38). Later on, OCT has been applied to imaging the gastrointestinal tract (32, 39, 40), coronary arteries (34, 35, 41,

42), embryonic heart (43), dermatology (44, 45), pulmonary medicine (46), gynecology (47) and many other applications.

1.2.1 Principles of OCT

Time Domain OCT

OCT measures the magnitude and echo time delay of backscattered or reflected light (31). OCT uses infrared light, which can penetrate tissues up to 1-2mm. Early time domain OCT system (TDOCT) is simply a modified Michaelson interferometer (48) (Fig. 1.2). The incident light is divided into two halves: one goes to a mechanically moving reference mirror, and the other half goes to a scanner to image the tissue. The two paths of light are either back-reflected or backscattered and recombined to interfere. A photo detector is used to detect the interference fringes. The coherence length of the light source determines the axial image resolution, i.e. only when the two paths of light travels with a difference within the coherence length can they interfere with each other. As broadband light sources used in OCT systems have very short coherence length, this provides "optical sectioning", generating high-resolution, high contrast depth-resolved images. Different depths of tissues can be simply obtained by scanning the reference arm and demodulating the interference signal. This is also known as A-scan, and the corresponding line signal is termed "A-line". By scanning the galvanometers in the X-Y dimensions, we can combine the A-lines in the other two dimensions and obtain 2-D and 3-D volumetric OCT images. As the reference mirror is mechanically moved, the speed of TDOCT system is typically low.

Fourier Domain OCT

The second generation OCT technology is Fourier domain OCT (FDOCT) (49-52). In FDOCT, the reference arm is fixed, and the depth-resolved images are obtained by detecting the interference spectrum in the Fourier domain and Fourier transforming it

back to the spatial domain (48, 53, 54) (Fig. 1.2). Because no mechanical scanning of the reference mirror is needed, FDOCT dramatically improves the imaging speed by more than 10 folds. As all the echoes of light are acquired simultaneously, FDOCT also has significant sensitivity advantages over TDOCT, demonstrated by three independent groups in 2003 (50-52). Based on different approaches to detect the interference spectrum, FDOCT can be divided into two types. The first type is spectral domain OCT (SDOCT), where a spectrometer and a high speed line scanning camera are used to detect the magnitude of interferogram at individual wavelengths simultaneously (55, 56). The second type is swept-source OCT (SSOCT) (57), or Optical Frequency Domain Imaging (OFDI) (58), where a rapidly sweeping laser is used to generate different narrow band frequencies of light, which are sequentially detected by a photo detector. SDOCT has a more stable phase response since all wavelengths of light are detected simultaneously. On the other hand, SSOCT can achieve much higher speed due to the ease of faster sweeping laser technology as compared to high speed line scanning cameras. In addition, the narrow band of swept source provides better roll-off than SDOCT systems. Ultrahigh speed and ultra-long coherence length SSOCT systems have become possible due to two representative light source technology advances in recent few years, namely Fourier domain mode locked (FDML) lasers (59) and vertical-cavity surface emitting laser (VCSEL) (60, 61), respectively. State-of-the-art FDML based swept source systems allows acquisition of multi-million A-lines per second (62, 63) and real-time (video rate)

22

3-D OCT volume rendering facilitated by Graphical Processing Unit (GPU) computing (64).

Detector

Time-domain OCT

Reference Mirror z

Fourier-domain OCT

Broad Bandwidth Light Source

Sample

Backscattered Intensity

Transverse Scanning

B-scan of New Zealand White Rabbit Left ventricle endocardium

sweeping lasers

Detector

Mirror

Sample

Sample

Broad Bandwidth Light Source
Reference Mirror

Detector

Reference

Wavelength

Spectral-domain OCT *Swept source OCT*

Figure 1.2. Schematic diagram of time-domain OCT, spectral-domain OCT and swept source OCT.

1.2.2 IVOCT

Intravascular OCT (IVOCT) is used to image the coronary arteries, and has now become the second most successful application just after ophthalmic OCT (48). Compared to free-space OCT systems, the difference of IVOCT is that the sample arm is made into a disposable imaging catheter that can be inserted into the coronary arteries. (Fig. 1.3) Typically, the catheter is connected to the IVOCT console through a rotary junction. Inside the catheter, a single-mode fiber is used to guide the light towards a micro-optical lens and a prism, which reflects the light for side-view imaging (65). The

first demonstration of *ex vivo* IVOCT imaging was performed by Tearney et al in 1996 (41). The first *in vivo* IVOCT imaging was demonstrated in a porcine model again by Tearney et al (42). OCT imaging in human patients was first reported by Jang et al (66).

Meanwhile, IVOCT has experienced a rapid, successful commercialization worldwide. The first generation TDOCT system, developed by Lightlab Imaging (now becomes part of St. Jude Medical Inc, St. Paul, MN), first hit the Japan market in 2007, and later in Europe. The system has a tiny image wire (0.019 inches), and uses balloon occlusion to displace the blood (30). The imaging speed is limited to 10-30 frames/s. The second generation Fourier domain IVOCT system C7-XR from Lightlab, approved by FDA in the US in 2010, is a SSOCT system with much higher imaging speed (100 frames/s and 20 mm/s pullback). This system is equipped with a 0.9mm diameter catheter, which is thicker than the earlier version, but is more stable and more rigid. The accelerated imaging speeds permit the use of a single, high rate (~4 cc/s) bolus injection of contrast to produce a blood-free environment, thereby eliminating the need for balloon occlusion (30). The first US IVOCT clinical case was performed by Dr. Marco Costa at the University Hospitals Case Medical Center (Cleveland OH) in May 2010. It is expected that the annual growth rate of IVOCT market will maintain around 60% through the year 2015, and will eventually catch up the current IVUS market (~800M).

Figure 1.3. Schematic diagram of intravascular OCT (courtesy from St. Jude Medical Inc. St Paul, MN)

Fig. 1.4 shows examples of both the cross-sectional (top) and the longitudinal view (bottom) image from a commercial IVOCT system (C7-XR, St. Jude Medical Inc, St. Paul, MN). IVOCT images are naturally acquired in polar coordinates (Fig. 1.4). After logarithmic compression, images are typically converted from polar to cartesian coordinate for display. However, as can be seen in later chapters, many image processing tasks can be performed more easily in the polar domain. Notice that due to the helical scanning pattern during imaging, the cross-sectional plane is actually oblique with respect

to the pullback direction. In commercial OCT systems, longitudinal view (L-mode) image is also used. It is obtained by combining all image pixels at the plane intersects the catheter center at one rotation angle (Fig. 1.4 bottom).
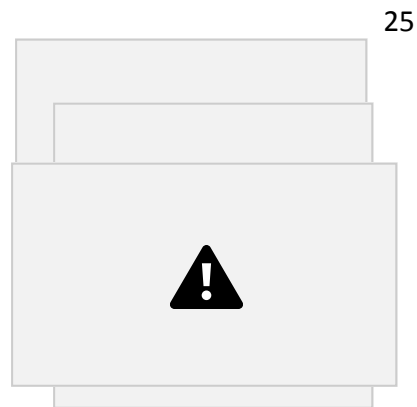
Figure 1.4. Examples of IVOCT images from a commercial FDOCT system (C7-XR, St. Jude Medical Inc, St. Paul, MN).

Fig. 1.5 illustrates the major vascular features that can be visualized by IVOCT. Lumen boundary is the distinctive vessel inner boundary. The vessel lumen size is a direct indicator of stenosis. Guide wire is commonly used during OCT imaging to guide the catheter through the coronary artery. It highly reflects light and creates a long dark shadow behind it in the image. Typically, guide wire artifact needs to be excluded for further processing. Calcified plaque presents as a signal-poor region delineated by sharp

boundaries (34). Lipid plaque (necrotic core) is a signal-poor region delineated by diffuse boundaries (34). It highly attenuates light, and therefore the abluminal boundaries of the plaque are usually not present in OCT images. Fibrous cap appear as signal-rich regions. If the thickness of the fibrous cap is less than 65μm, the plaque is often referred to as thin-cap fibroatheroma (TCFA). Rupture of TCFA is believed to cause most of the acute coronary events. Metallic stents strongly reflect light and manifest as bright reflections coupled with dark shadows in OCT images (Fig 1.5 (B)).

26
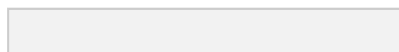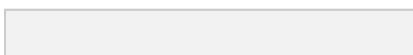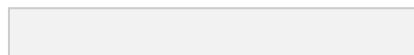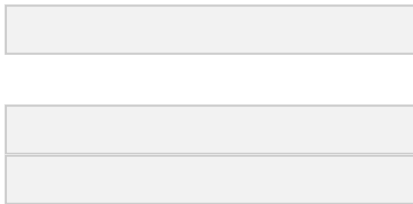
Figure 1.5. (A) Atherosclerotic plaques in IVOCT images. (B) Metallic stents in IVOCT images.

1.3 IVOCT Image Analysis

1.3.1 Manual vs. Automated Image Analysis

In order to derive quantitative information for research and diagnostic purposes, IVOCT images have to be processed either manually or automatically. Typical IVOCT image processing tasks include image segmentation, feature quantification, object detection, and tissue characterization. Currently, IVOCT image processing has been mainly conducted manually by human analysts. There are three limitations associated with manual image processing. First, it is tedious and extremely time-consuming. One important reason contributing to the time-intensive analysis is that one IVOCT pullback usually contains hundreds of images for analysis. In addition, some IVOCT image processing tasks are in nature labor-intensive. For example, to quantitatively assess stent strut coverage, one need to manually mark hundreds or even thousands of stent struts in one pullback, and this usually takes more than 7 hours. Another example is segmentation of calcified plaques. In this task, human analysts need to manually delineate the plaque contours in all the frames using a mouse or equivalent tools.

The second limitation is that there could be significant inter-observer variability associated with manual analysis. For instance, to measure the minimum fibrous cap thickness, different analysts may make measurements at different positions on the fibrous

cap boundaries due to visual uncertainties and their measured cap thicknesses may differ significantly. One study shows that when three analysts independently assessed the minimum cap thickness of the same 14 lesions, at least one of them gave a different call on TCFA in 10 out of 14 lesions (67).

Third, the quantitative metrics that can be computed manually are limited by the available functionality provided by the commercial software. Many potentially relevant metrics, in particular for research purposes, are almost impossible to be generated using commercial software. Many image processing tasks are hard, and require extensive research and validation before commercially available.

Most of the limitations discussed above can be addressed by automated or computer aided image analysis. First, automated image processing method will significantly reduce the image analysis time. For instance, image processing methods may reduce the stent analysis time from > 7 hours down to minutes. This will on one hand enable analysis of large clinical trials, and on the other hand make it possible to provide physicians live time feedback during stent deployment. Second, automated image analysis can effectively reduce the inter-observer variability of certain tasks. For instance, using computer-aided method, the minimum fibrous cap thickness can be determined more accurately and consistently because once the fibrous cap boundary is determined, there is no uncertainty for the computer to determine the minimum cap thickness. Third, automated image processing allows some quantitative tasks that are otherwise

impossible. For example, quantification of macrophages is a challenging task for human analysts because macrophages are too small and easy to be misidentified as lipid crystals

or speckles with similar signatures (36, 68). After systematic training, a computer-aided method can provide a consistent scheme for macrophage detection and quantification (36, 69). Another example is that computers are generally good at performing 3-D image processing tasks such as 3-D visualization, 3-D object segmentation and quantification. Human analysts are not used to performing such tasks manually.

1.3.2 Previous Work

IVOCT has just been applied to clinic several years ago, and IVOCT image analysis is still at its infant stage. During the past few years, there are a number of automated image processing methods reported, most of which are focused on lumen contour detection, stent analysis, and tissue characterization. We next review some representative work in each area.

Several studies have been reported on automated lumen segmentation. Sihand et al (70) used simple edge detection and edge linking for lumen segmentation. However, the edge thresholding and linking step is very ad-hoc and may fail in noisy images. Gurmeric et al (71) proposed a spline based active contour method which requires an initial contour generated by thresholding. Thresholding suffers from similar problems and the active contour model may converge to a local, instead of the global optimal boundary. Ughi et al (72) used A-line analysis and spline fitting for lumen segmentation. However, single A-line analysis does not incorporate spatial correlation between adjacent A-lines naturally and therefore is noisy. Tsantis et al (73) proposed a Markov random field (MRF) model that optimizes a cost function at pixel level involving interaction of

neighboring pixels in an iterative manner. However, local regional optimum does not

necessarily correspond to the global optimum for the entire lumen boundary. In addition, this study did not use clinical IVOCT images. In summary, a fully-automated method that is able to robustly segment the lumen boundaries in clinical IVOCT images still merits research and investigation. One aim of this dissertation is to develop a 3-D optimal lumen segmentation method with robust performance in clinical IVOCT images and at the same time can be operated near real-time during clinical procedures.

Several studies on metallic stent detection in OCT images have been recently reported (71-77). While differing in specific methods, studies (71, 72, 74, 75, 77) have all employed single A-line analysis or 2-D edge detections to capture the signatures of individual struts (i.e. bright reflections and shadows). Commonly in these methods, a large number of empirical parameters and thresholds have been used. As the intensity and contrast of OCT images can vary from pullback to pullback, and various artifacts may be present, methods with hardcoded empirical parameters are difficult to generalize in practice. Later studies have used feature extraction and classification techniques to facilitate stent detection. Tsantis et al (73) applied probabilistic neural networks to detect stent strut based on a variety of strut features extracted using continuous wavelet filters. However, as this study has used images acquired from femoral arteries, and has not directly compared the strut detection to the gold standard, the performance of the method in clinical intracoronary OCT imagers is unknown. Lu et al (77) applied bagging decision trees as the classifier on initial screen of candidate struts, and has achieved promising results in the a small number of validation set. Such classification-based methods can take advantage of human expert knowledge, and can easily combine multiple features for

30

decision making, and are therefore potentially more robust. Study (76) is focused on a restricted category of cases where stent struts lack typical bright spot and shadow appearance, but appear as elongated ridges due to very thick tissue coverage. Therefore, a 2-D ridge detector has been proposed (76). All these studies (71-77) have only used local features of individual struts for strut detection, without considering any high-level information, such as a spatial constraint between adjacent struts. Validation studies of all these methods have been typically conducted employing less than 10 pullbacks. Although promising results have been achieved in the limited data sets selected in these studies, the generality of these methods to large numbers of clinical data sets have not been demonstrated. One aim of this dissertation is to develop a 3-D method that can take the higher level stent shape information into account for more robust stent strut detection.

Optical properties of tissues can be used to characterize and classify different tissue types. There are two representative studies reporting computer-aided tissue characterization. Xu et al (78) proposed a single scattering model to extract the backscattering and attenuation coefficients of tissue. Consider a single A-line with *P(z)* representing the power of signal at depth *z*. The single scattering model can be represented as

$$\log(P(z)/P_0(z)) = \log(\mu_b/\mu_{b0}) - 2\mu_t z/n \qquad (1)$$

Where μ_b and μ_t are the backscattering and attenuation coefficients, respectively. $P_0(z)$ and μ_{b0} are measured from phantoms with negligible attenuation coefficient, and are used to cancel light source specific beam parameters. *n* is the refractive index of the tissue. After the IVOCT image is logarithmically compressed, a straight line can be least square fitted to the A-line profile, and the intercept and slope are proportional to the

backscattering and attenuation coefficient, respectively. As specular reflections and noises can both affect the fitting, according to (78), the fit is restricted to region from 50μm below the surface to the point where the signal is attenuated 1/e of the starting point. Results from this study demonstrate that fibrous plaques have high backscattering and low attenuation, calcified plaques have low backscattering and low attenuation, and lipid plaques have high backscattering and high attenuation. Therefore, plaques can be classified by combining both backscattering and attenuation coefficients. However, the above numbers are derived from transversal scanning OCT on paraffin embedded sections, instead of radial scanning pattern used in clinical IVOCT. van Soest (79) proposed a similar single scattering model and applied it to rotary IVOCT. Attenuation coefficient of every A-line is extracted, with additional considerations of tissue discontinuity. Similar attenuation coefficients were found for the major types of plaques. The entire image can then be colorcoded with the attenuation map. More complex multiple scattering models have also been proposed (80, 81).

Tissue characterization using optical properties provides physical explanations of the image formation for various tissues, and can be verified by experiments. However, directly applying the method to the original image is noisy, as only single A-line or averaged A-lines are used without considering the regional/global information of the image. Selection of regions of interests for analysis is important but this is often performed manually. Image segmentation methods can help constrain the model fitting in single type tissues and will help improve the performance of the methods. In this dissertation, we developed a variety of image segmentation methods for different vascular features.

1.3.3. Overview of Automated IVOCT Image Analysis

Fig. 1.6 summarizes the automated IVOCT methods developed in this thesis work. These methods include algorithms for existing applications but are potentially more robust than previously published methods, such as lumen segmentation and stent analysis. Additionally, we also explored some novel applications such as segmentation of calcified plaques, and volumetric quantification of fibrous caps. Among these methods, catheter segmentation, lumen segmentation and guide wire segmentation serve as the common pathway and the basis for more advanced plaque and stent analysis. Catheter segmentation is a prerequisite step for calibration of IVOCT images. Lumen boundary is essential to locate plaque and stent struts in an image, and the centroid of lumen is often used as the reference for quantification. Segmentation of calcified plaques and fibrous caps is the basis for comprehensive quantification of calcium and TCFA, respectively. Once the fibrous cap boundaries are segmented, macrophage quantification can be performed within the fibrous caps. Automated stent strut detection is the basis for assessing stent strut coverage and tissue responses. Collectively, all the vascular features segmented/detected by the proposed methods can be reconstructed and visualized in 3-D, providing augmented "virtual histology" to advance our understanding of the mechanisms of CAD and to help guide PCI. It is important to note that these methods cover the most common image processing work performed in the Cardiovascular Core Labs. Some other important tasks such as thrombosis characterization, although not covered, can still benefit from one or more methods proposed in this thesis (e.g. lumen segmentation can be used as the basis for thrombosis segmentation). In addition to the

image analysis methods, we also develop a prototype software package OCTivat (intravascular OCT image visualization and analysis toolkit) for researchers and

physicians as the powerful tool for IVOCT image visualization and analysis. In the following chapters, we will discuss the specific algorithms developed for each application. For each application, we also provide extensive validation experiments to demonstrate the performance of the algorithms. Finally, we address the clinical relevance of each method and discuss the future improvement, if possible.

Input Volumetric
OCT Images

Vessel
stenosis

Common

Pathway

Z-offset calibration

Plaque and Stent
analysis

Research, diagnosis
and treatment of
coronary artery
diseases

Image Visualization and
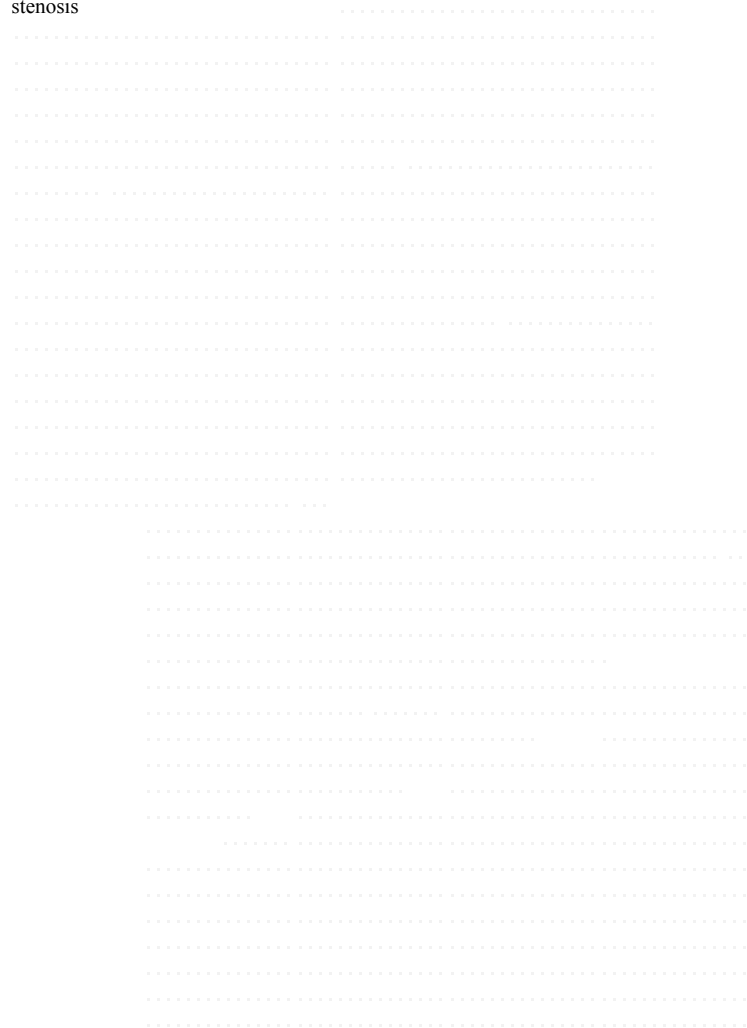Analysis Software
Software Development

Figure 1.6. Overview of the automated image processing methods developed in this thesis

Chapter 2. Automated Segmentation of Lumen, Guide Wire, and Catheter Boundaries

2.1 Lumen Segmentation

Lumen segmentation is often the basis for more advanced plaque and stent analysis. In addition, lumen area itself is a direct indicator of vessel stenosis. In OCT images, luminal boundary is very distinctive and it is likely that many image processing techniques can succeed in this task (70-73). We describe two methods here, and both have been proved to be robust in practice. The first method is a 2-D optimization method using dynamic programming (67, 82), and the second one is a 3-D optimization method using closure graph and graph-cut (83). Later one can see that, the basic principles of the two methods can be easily extended to other applications.

2.1.1 2-D Dynamic Programming Method

Searching for the vessel luminal boundary in the polar coordinates of OCT images fit the graph search family of optimization problems naturally. The lumen boundary is unique and the accumulated optical intensity difference between the pixels from the vessel and luminal side along the contour is maximum. The global optimal boundary can be efficiently found using a classic optimization method, dynamic programming (DP).

DP is a general technique used to solve certain optimization problems [21]. The basic concept is to find the globally optimal solution to the original problem by building on optimal solutions to subproblems. Once the subproblem is solved, the solution is cached for future look-up. Therefore, redundant computations can be avoided. It is very robust in

the presence of noise and this is attractive to OCT image analysis because OCT images often suffer from speckle noise and various artifacts.

Consider the OCT images in polar coordinates (θ, r) where θ is angle and r is depth. Suppose there are *m* A-lines in one image. We assign each pixel at row *i* and column *j* an objective function *f(i,j)* favoring the characteristics of lumen. Our goal is to search for a path from row 1 to row *m* with the optimal cost *C*. We can break the problem into subproblems such that the path to row *i* is always coming from the path to *i-1* with some connectivity constraint. Therefore, we have the following recursive function:

$$
C(i,j) =
\begin{cases}
f_{ij} + \max_{\substack{j-n \le j^* \le j+n}} \{C(i-1, j^*)\} & 1 < i \le m \\
C(i,j) = f(i,j) & i = 1
\end{cases}
\tag{2}
$$

Where *C(i,j)* is the accumulated cost from row 1 to point *(i,j)*, *j** is adjacent to j and *n* specifies connectivity. The globally optimal boundary can be found by selecting the point in row *m* where the accumulated cost is maximum and back tracking the path (67, 82). *f(i,j)* can be simply defined as the intensity difference between image pixels on the vessel and luminal side.

$$
f(i,j) = I(i, j) - I(i, j'), \quad j - w \le j' \le j, \; j < j'' \le j + w
\tag{3}
$$

where *I* refers to the average of pixel value, and *w* is the length of the window for averaging. When the guide wire stays close to the lumen boundary, its bright reflections may obscure the lumen boundary and need to be excluded from lumen segmentation. This can be achieved by guide wire segmentation introduced in Section 2.2. For image

segmentation, the advantages of DP include the global optimum nature, simplicity and

stability. The limitation is that it is not easy to be generalized to 3D or higher dimensional space.

2.1.2 3-D method: Surface Segmentation Using Graph Cut

The 3-D lumen segmentation method is based on the surface segmentation method proposed by Kang et al (84). It is worth mentioning that this method has been successfully applied to intraretinal layer segmentation in ophthalmic OCT images by Garvin et al (85, 86). The main idea of the method consists of two steps. First, the volumetric images are transformed into a closure graph, where the optimal closed set corresponds to the optimal surfaces in the original images. The second step is to search for the optimal closed set using graph cut algorithms. We next introduce the method in the IVOCT context.

We denote a voxel V in the IVOCT pullback as $V(z,\theta,l)$, where $z,\ \theta,\ l$ are the coordinate in the axial, lateral and longitudinal direction, respectively. We first look at how we can transform the image stack into a closure graph according to the work by Wu et al (87) and Kang et al (84). Consider a directed graph $G=(V, E)$ with nodes V and edges E. Each node is formed by a voxel in the IVOCT pullback in the polar coordinate. Each node is associated with a weight $c(z,\theta,l)$ (*node weight*) penalizing the probability of it being located on the lumen boundary, taking the form defined in Eq. (3).

We denote the farthest plane from the catheter in the IVOCT pullback as the *base layer* ($z=0$). Then the top plane (closest to the catheter) is represented by $z=N-1$, where N

is the number of points in each A-line. If we define the cost of a surface as the total weights of all the nodes on the surface, the optimal luminal surface has the minimum cost

among all the possible surfaces. To construct a closure graph, we change the *node weight* from $c(z,\theta,l)$ to $w(z,\theta,l)$ as follows:

$$w(z,\theta,l) = \begin{cases} c(z,\theta,l) & z=0 \\ c(z,\theta,l) - c(z-1,\theta,l) & z>0 \end{cases} \quad (4)$$

Each node $V(z,\theta,l)$ on layer $z=1,\ldots N-1$ has a direct edge with infinite weight linked to $V(z-1,\theta,l)$. The purpose of these edges is to guarantee the detected surface intersects each A-line exactly once. We further denote $_{adj}\theta$ and $_{adj}l$ as the sets of adjacent A-lines of θ and adjacent frames of l, respectively. We then make a direct edge with infinite weights linking V to the farthest node it could reach in every adjacent set under some smoothness hard constraint Δz:

$$E_{hard} = \{(V(z,\theta,l), V(\max(0,z-\Delta z),\theta_{adj},l_{adj}))\} \quad (5)$$

The hard constraints prevent the height of the surface from adjacent A-lines/frames differing more than Δz, therefore enforcing smoothness. Notice that we can incorporate the special helical scanning pattern of IVOCT into the neighborhood definition, i.e., the last A-line in frame i is adjacent to the first A-line in frame $i+1$. In addition to the hard constraints, soft constraints (88, 89) are also added as direct edges linking a node to the node immediately lower than it in adjacent A-lines/frames:

$$E_{soft} = \{(V(z,\theta,l), V(\max(0,z-1),\theta_{adj},l_{adj}))\} \quad (6)$$

The soft edges are assigned finite edge weight w_{soft} .Soft constraints will not prevent, but will impose a penalty if the surface height changes dramatically. Finally, we make the *base layer* strongly connected using infinite edges (every node in this layer is reachable from any other node). Now, one can see that the optimal surface of the original IVOCT pullback corresponds to the optimal closed set (constituted by all the nodes on and below

the surface) in the graph G (84, 87). To verify this, observe that when adding the cost of all the nodes below a feasible surface, all the node cost will be canceled out except for the nodes on the surface. Further, as any successors of any node in the set are still in the set, the set is a closed set. This transform allows us to solve the original problem by equivalently searching for the optimal closed set in the graph.

Searching for the optimal closed set in a graph can be efficiently solved using max flow/min-cut algorithm, as shown by Picard in 1970s (90). Briefly, we construct a closure graph G^C from G by adding two special nodes source s and sink t. We create directed edges linking s to all the nodes with negative weights, and edges connecting all nodes with positive weights to t, with the *edge weight* equal to the absolute value of the *node weight*. For any other edge connecting two non-s/t nodes, we assign them infinite *edge weight*. A cut in a graph partitions the graph into two disjoint sets containing s and t, respectively. The minimum cut is the cut where the sum of edges it severs is minimum. The minimum cut is also a finite cut, and can only sever finite edges connected to *s/t* in G^C. One can easily prove that (90, 91), after a finite cut, the set containing s becomes a closed set and the optimal closed set corresponds to the minimum cut of this closure graph.

The surface segmentation method above is ideal for robust 3-D lumen segmentation

due to its global optimum nature. However, the time and space requirement of the method is huge. For typical IVOCT image stack consists of 500*1000*271 pixels, the constructed graph requires >10G memory. It takes tens of hours for state-of-the-art graph algorithms to compute the optimal surface, which is impractical for practial applications. We can use a simple multi-resolution approach (92) to overcome this computation burden effectively.

39

Consider a coarse-level image stack obtained by downsampling the original image stack in axial and lateral directions (Fig. 2.1). As the lumen boundary is very distinct, it still remains the global optimal boundary although some details were lost in the coarse level. We can perform graph cut to obtain the optimal surface $_cS$ at this coarse level, and project it back to the original fine level, denoted by $_fS$. We know that, the true optimal surface $_f^*S$ should be close to $_fS$. Hence, we can perform the second round graph cut on the fine level, but only consider the voxels within a narrow band $_fS\,d \pm$ surrounding $_fS$. By computing the optimal surface twice, but at different resolution, the total computation time can be significantly reduced.

One potential problem of the surface segmentation is that the computed optimal surface might be an empty set, which is not what we desired. This problem happens very frequently at the second round graph cut at the fine level, where only a narrow band of pixels are used. When this happens, the minimum cut is simply to cut around the source *s,* which becomes an isolated set. We propose a simple solution to the problem. Notice that ideally in the solution, the *base layer* should always be contained in the closed set. Thus, we simply "strengthen" the connection between the *base layer* and *s* by assigning a very large weight to all the nodes connected to *s* in the *base layer*. We empirically found

that this simple solution is able to completely fix the empty closed set problem. Regarding other possible solutions, Wu et al (87) proposed a "translation" procedure where the weight of one arbitrary node in the *base layer* is decreased by *M*+1, where *M* is the total weight of the *base layer*. However, we found this approach did not work, at least tested by our problem.

40

Figure 2.1 Efficient segmentation of the optimal 3-D lumen boundaries using a multi-resolution approach. A coarse level IVOCT pullback was generated by downsampling the original high resolution pullback in the axial and lateral dimensions. Graph cut was performed to extract the optimal lumen boundaries on the coarse level, which was then mapped back to the fine level. A second round graph cut was performed on the fine level, but is restricted to the narrow band voxels sounding the mapped surface (yellow dotted lines). Using this two-step approach, the computation time can be reduced from tens of hours down to seconds.

Remark: distinction should be made between this surface segmentation method and the general graph cut method used for image segmentation proposed by Boykoy et al (93, 94). The major difference lies in the graph construction stage. The surface segmentation method uses closure graphs, and strictly separates the nodes above the below the surface. Therefore, it is limited to terrain-like surfaces (84). In comparison, general graph cut (93,

94) does not uses closure graphs, and it allows for segmentation of contours/surfaces with arbitrary shape, but typically requires user input of seed points indicating the foreground and background. Despite these differences, the same graph cut algorithm can be used in both methods. As IVOCT images are naturally acquired in polar coordinates, the surface segmentation method can guarantee the terrain-like lumen surfaces for the optimal

solution. However, it is important to note that the general graph cut is a powerful, globally optimal N-D segmentation method, with a wide range of applications in computer vision. More details of the method can be found in (93, 94).

2.2 Guide Wire Segmentation

We describe a guide wire segmentation method that is able to extract the global optimal guide wire positions of all the frames in the entire pullback at once (67, 82). Briefly, we create an *en face* projection image where 2-D images of the pullback are projected to 1-d curves and combined into one image (Fig. 2.2(b)). The regions of guide wire shadow become a continuous dark band. Similar to lumen segmentation, an objective function of pixel value difference is applied to the two boundaries of the dark band, but with different signs. DP is then applied twice to find the two boundaries. More robustly, the two coupled boundaries can also be found simultaneously using multiple surface segmentation technique in higher dimensions (84), or higher-dimension DP (95), but at the expense of increased computation time. The above described method only applies to OCT pullbacks with a single guide wire. Sometimes, there could be more than one guide wires inserted in the same vessel. In such cases, the *en face* view image can be combined with other methods for guide wire segmentation.

θ

z
θ

Figure 2.2.
Segmentation of
guide wires using
the *en face* projection view. (a) An cross-section image of a pullback showing the guide wire region with a
long dark shadow. (b) The *en face* projection view showing

42

the guide wire region as a continuous dark band traversing the whole pullback. The white dotted line
illustrates the position of the frame (a) in the pullback. The guide wire positions of all frames can be
simultaneously found by segmenting the two boundaries of the dark band.

2.3 Automated Calibration of IVOCT Images

During IVOCT image acquisition, due to fiber stretch and temperature fluctuations,

the optical length of the sample arm may vary. As a result, the apparent size of the

catheter could be smaller or bigger than the actual size (30). Therefore, it is important to

perform the so called "Z-offset correction" to adjust the image such that the size of

catheter matches that of the actual number. This is equivalent to translating the reference

arm of the IVOCT system to match the optical path length of the sample arm. Fig 2.3

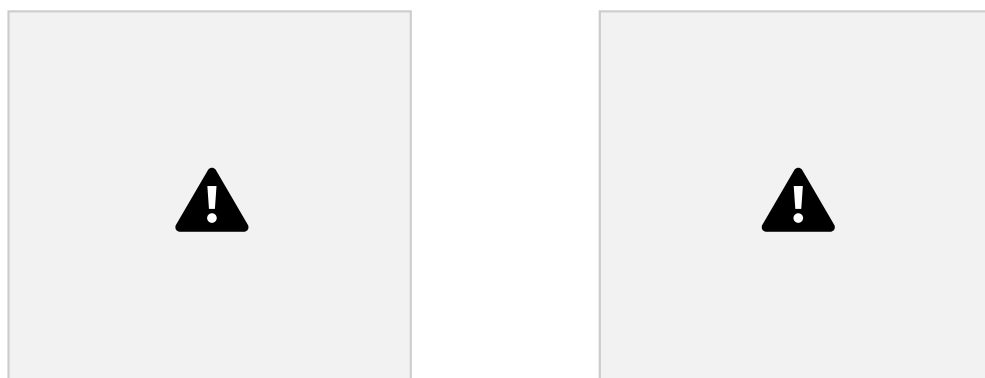illustrates examples of under-adjustment and over-adjustment of Z-offset.

Figure 2.3. Under-adjustment (left) and over-adjustment (right) of z-offset in IVOCT images. Top: Cartesian coordinate; Bottom: corresponding polar coordinate.

The key idea for automated Z-offset calibration is to detect the catheter boundary accurately. Then we can adjust boundary to match the *a priori* catheter size. However, there are several boundaries inside the catheter, including the boundary of the imaging

probe, and boundaries of the plastic sheath surrounding the probe. We propose using the two coupled boundaries of the plastic sheath for calibration. First, using the plastic sheath is more reliable as compared to other boundaries as it is always the outmost layer. It is also the feature used by human analysts for manual Z-offset calibration. Second, the two coupled boundaries is a more robust signature than the single outmost boundary. One can appreciate the fact that, if an algorithm is designed for only the single outmost boundary of the sheath, the detected boundary may cross between the two boundaries as both have very similar features. It turns out that we can use the same surface segmentation algorithm (Section 2.2.2), but with additional considerations of the inter-surface constraint between the two boundaries. (Fig. 2.4) Specifically, for each node in surface 1, we make a directed edge to the farthest (highest) node it could reach in surface 2. Correspondingly, for each node in surface 2, we make a directed edge to the closest (lowest) node it could reach in surface 1. The detected coupled two boundaries will be constrained between these two constraints, i.e., they are neither too close nor two far apart, thereby respecting the physical distance between the two boundaries.

2.4 Experimental Studies

We mainly evaluated the accuracy of lumen segmentation in this dissertation, leaving the validation of catheter segmentation in future work. During PCI, the choice of the strategy and the specific devices (coronary balloon and stents) relies on measurements obtained from lumen segmentation. The most common metrics used are Minimal lumen area (MLA) and reference vessel diameters. If stenting is necessary, physicians will tend to implant a stent covering the MLA region to recover the bottleneck of the blood flow.
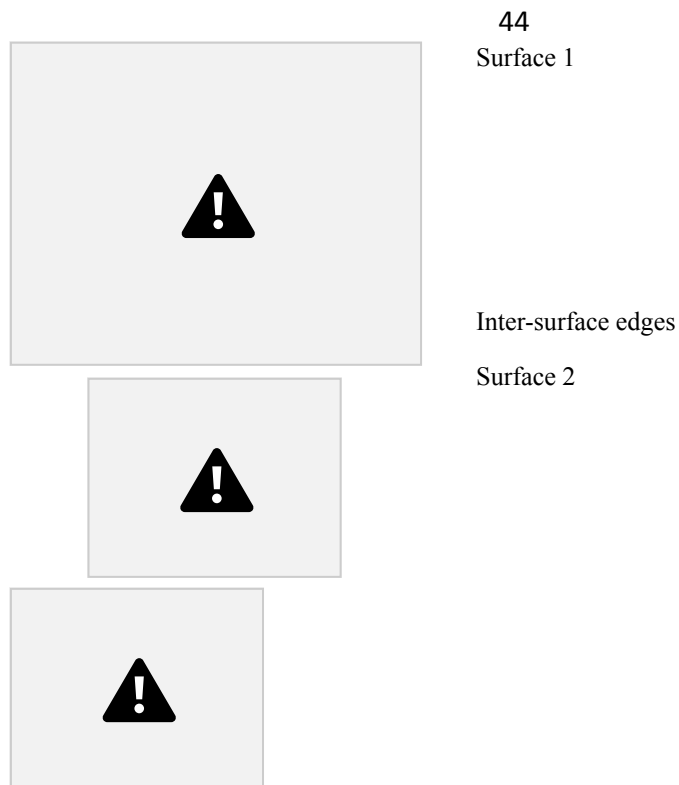
Surface 1

Inter-surface edges

Surface 2

Figure 2.4. Left: Automated IVOCT calibration as detecting two coupled boundaries of the plastic sheath

outside the imaging probe. Right: Graph construction with inter-surface edges to constraint the two surfaces neither too close nor too far apart. The red dotted curve represent potential feasible surfaces.

We first evaluated the accuracy of the clinical metrics determined by the algorithm, namely MLA and vessel diameters. For comparison purposes, two independent experienced OCT analysts performed offline manual segmentation of lumen area at two different time points in the 62 cases. Analysis was performed using commercially available offline analysis software (St Jude Medical, St. Paul, MN). One analyst first determined the longitudinal region of interest (ROI) by specifying the starting and ending frame for analysis, and the same region was used for both analysts to search for the MLA. At the area of suspected MLA, lumen tracing were performed every frame with careful manual correction and the frame with the smallest lumen area was chosen as the MLA. The minimum, mean and maximum lumen diameters were also calculated using the commercial software at the MLA frame. To evaluate intro-observer variability, both analysts re-performed the same task on the same data after two weeks. A third analyst reviewed all tracings and all three analysts decided on the "gold standard" MLA and the

45

corresponding vessel diameters. The algorithm was applied to all consecutive images of the longitudinal ROI of the 62 cases, including 11468 images in total (average 184±58 frames/pullback), and automatically determined the MLA and the vessel diameter.

We then assessed the general lumen segmentation accuracy of the method. For validation, 355 images randomly selected from arbitrary 20 pullbacks were manually segmented by one experienced OCT analyst. To ensure randomness, images at a 10- frame interval at frame numbers of multiples of 10 were strictly extracted from the longitudinal ROI, regardless of image quality and artifacts. Dice's coefficient (DSC) was used to

assess the agreement, defined as $DSC=2|A \cap M/(|A|+|M|)$, where A and M indicate the automatic and manual segmentations, respectively. A DSC value of 1 indicates perfect agreement. We also compared our method with one of the state-of-the art method employed in the commercial software (Version C.0.4, St Jude Medical) in the same 355 images. The commercial method is a frame-by-frame based segmentation method and is therefore representative for previous 2-D methods, and is one of the most widely used methods for IVOCT lumen segmentation worldwide.

The major parameters in the surface segmentation method are the smoothness hard constraintΔz and soft constraint w_{soft} .For adjacent A-lines, we set Δz to be 9 and 5 for the 1st and 2nd round graph cut, respectively. For adjacent frames, we set Δz to be double the value in adjacent A-lines as the frame interval in the current IVOCT system is large ($200\mu m$). w_{soft} was determined as 0.001 experimentally. The window width w in Eq. (3) was chosen to be 0.1mm, and the band width d in the 2nd round graph cut was set to be 7 pixels. We have found that further increasing the band width d has almost negligible

46

improvement on the segmentation performance, but will increase the computational burden significantly.

2.5 Results

Fig. 2.5 shows the accuracies of the MLA frame selection represented as the selected frame differences with reference to the gold standard. Most of the MLA frames determined by the algorithm agree with the gold standard, and this agreement is better than human analysts. In fact, from Fig. 2.5, it is clear that human analysts can sometimes be very far from the gold standard. In particular, comparing to human analysts, the

algorithm determined higher percentage of selected MLA frames with no difference or within 1mm away from the gold standard, but lower percentage of frames of >1mm differences (Fig. 2.5 (b)). Bland-Altman plots (Fig. 2.6) shows that the algorithm has no clear bias for determining MLA and mean lumen diameters, although a slight bias exists for minimum and maximum diameter, which is also present between the two analysts and gold standard. The average differences between the algorithm and gold standard in determining MLA, minimum, mean and maximum lumen diameters are $0.15\pm0.14mm^2$, $0.28\pm0.29mm$, $0.06\pm0.06mm$ and $0.32\pm0.27mm$, respectively. The disagreement between the algorithm and the gold standard is smaller for all the metrics as compared to both the human analysts (Fig. 2.6). The intra-observer variability for analyst 1 in assessing all metrics is $0.15\pm0.19mm^2$, $0.08\pm0.12mm$, $0.05\pm0.07mm$ and $0.08\pm0.10mm$, and for analyst 2 is $0.15\pm0.18mm^2$, $0.21\pm0.14mm$, $0.24\pm0.20mm$ and $0.10\pm0.14mm$.

47

200
Auto

standard

Percentage of selected frames with no difference vs. the gold

150 100 50

0

-50
Analyst1 Analyst2

Percentage of selected frames with a difference of 1-5 vs. the gold standard
Percentage of selected frames with a difference >5 vs. the gold standard

0 10 20 30 40 50 60 70 -150 Lesion Number
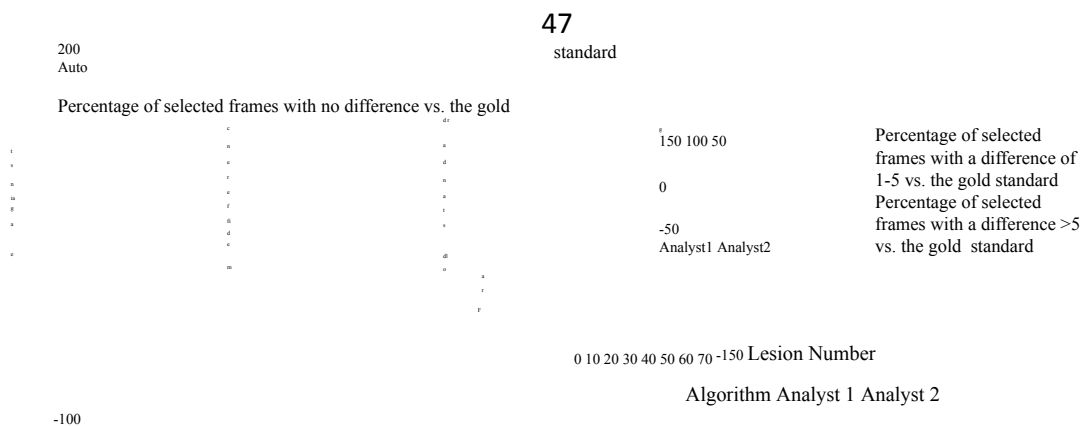
Algorithm Analyst 1 Analyst 2

-100

Figure 2.5. Comparison of the accuracy of the selected frame for assessing MLA between the algorithm and two experienced IVOCT analysts. Left: the selected frame difference against gold standard of the algorithm and two analysts in the 62 pullbacks. Right: The percentage of selected frames with no

difference, 1-5 frame difference (≤ 1mm) and >5 frame difference (> 1mm) difference against gold standard.

Figure 2.6. Bland-Altman plot of the MLA, minimum, mean and maximum lumen diameters determined by the algorithm and the two analysts, with reference to the gold standard.

48

For general lumen segmentation, the Dice coefficient between the automatically

segmented lumen and the gold standard over 355 images from the 20 pullbacks is 0.97±0.04. In comparison, the accuracy for the commercial software in segmenting these images is 0.95±0.05. In 3 out of the 355 images, where either the vessel lumen is extremely small or the image contrast is very low, the commercial software failed to generate any contours, and these images had to be excluded from the comparison. Paired t-test shows that our algorithm is significantly more accurate than the commercial software ($p<0.001$). Although in most good quality images, the commercial software and the 3-D algorithm had comparable performance, the 3-D algorithm is more accurate in the following situations. The first scenario is when the image is with significantly luminal blood. Luminal blood is a common artifact in clinical IVOCT images and will strongly attenuate light and degrade the image contrast, making the lumen delineation more challenging. In such cases, the commercial software can perform poorly (Fig. 2.5 (a)), but not the algorithm (Fig. 2.7 (b)). The second circumstance is that when the guide wire is contacting the lumen boundary, the commercial software often erroneously includes the guide wire as part of the lumen contour. In comparison, as the guide wire artifact is taken care of separately, the proposed method can smoothly interpolate the missing lumen contour. Finally, the commercial software is sometimes not precise enough in tracing the lumen boundary, as illustrated by the arrow in Fig. 2.7 (c), possibly due to excessive spline smoothing. By contrast, our algorithm just exactly follows the lumen boundary because the smoothness regulation has been already taken care in the graph construction, and no extra smoothing is performed on the contour. Fig. 2.8 shows some more examples of the automated lumen segmentation. The proposed method is able to accurately

49

segment lumen boundaries in large vessels (Fig. 2.8 (a)), in post-stenting pullbacks (Fig. 2.8 (b)), in vessels with severe stenosis (Fig. 2.8 (c)) and in images with artifacts of severe luminal protrusion (Fig. 2.8 (d)).
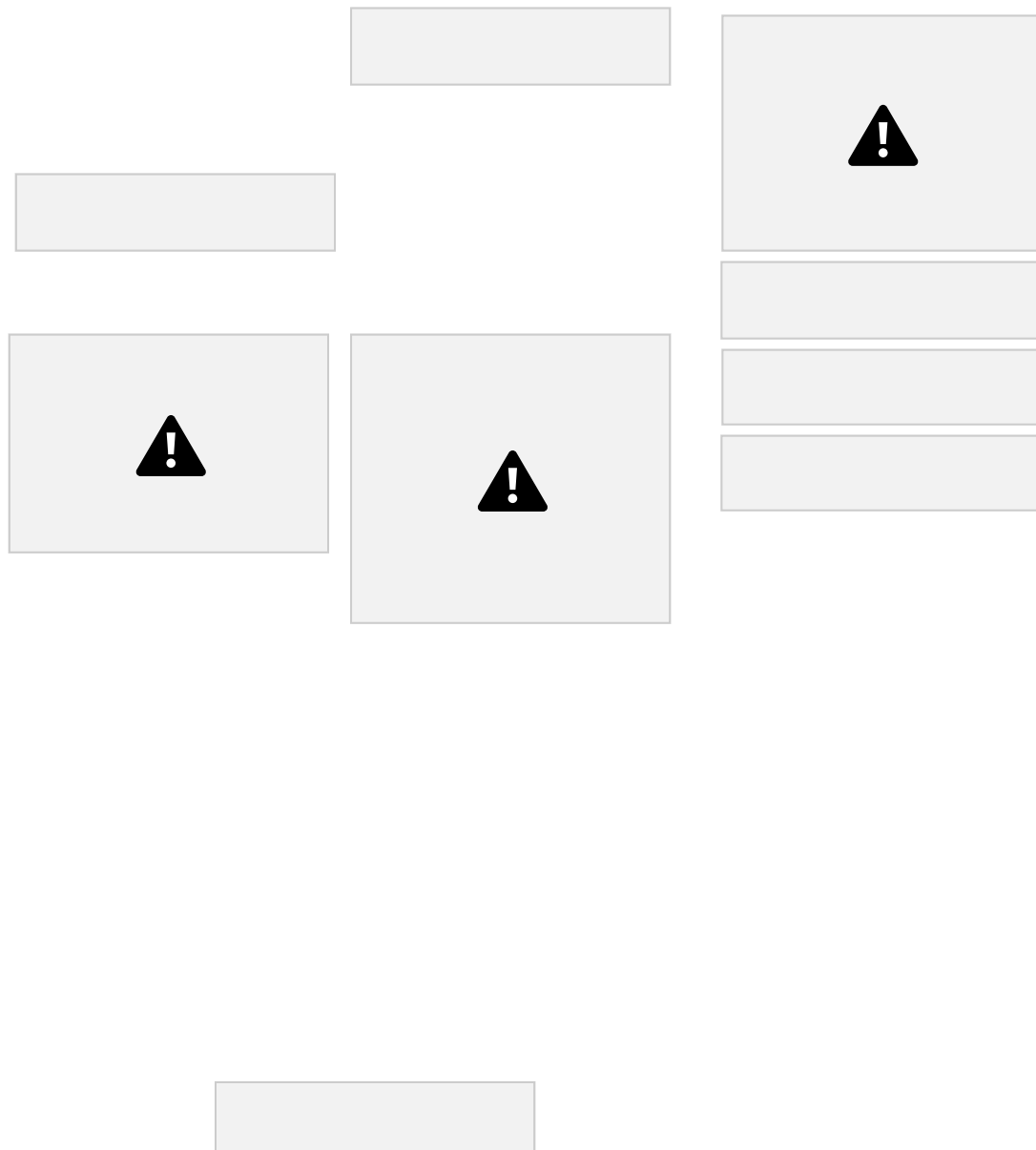
Figure 2.7. Comparison between commercial software and the proposed method in automated lumen segmentation.

Figure 2.8. Examples of the automated lumen segmentation. (a) Large vessel. (b) Post-stenting case with thin neointima coverage. (c) Severe stenosis with the guide wire touching the lumen boundary. (d) Luminal protrusion artifacts.

Fig. 2.9 illustrates how the automatic lumen segmentation algorithm can help provide extra useful information in addition to MLA. As the luminal boundaries in every frame are segmented, the whole vessel can be 3-D rendered with a plot of its luminal area at

each position side by side. In this example, the calculated MLA position is located at region B. Meanwhile, region A also has a very small luminal area (but larger than MLA) and may be disregarded if only single frame numbers are observed. However, region A is proximal to region B, and might be hemodynamically more significant than region B (expected distal vessel tapering).
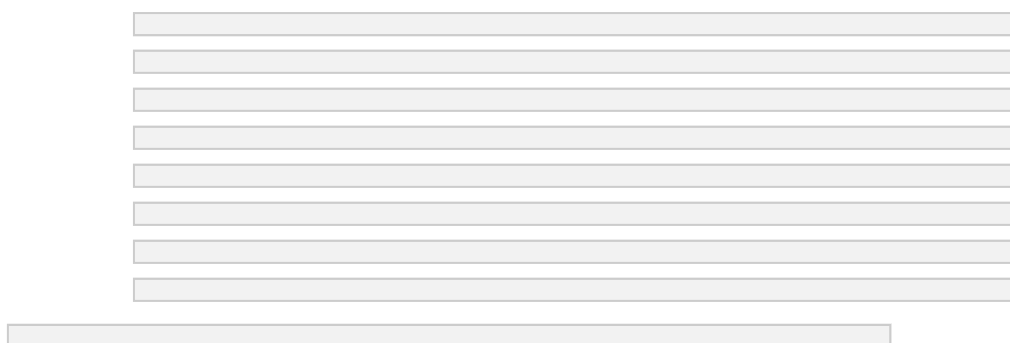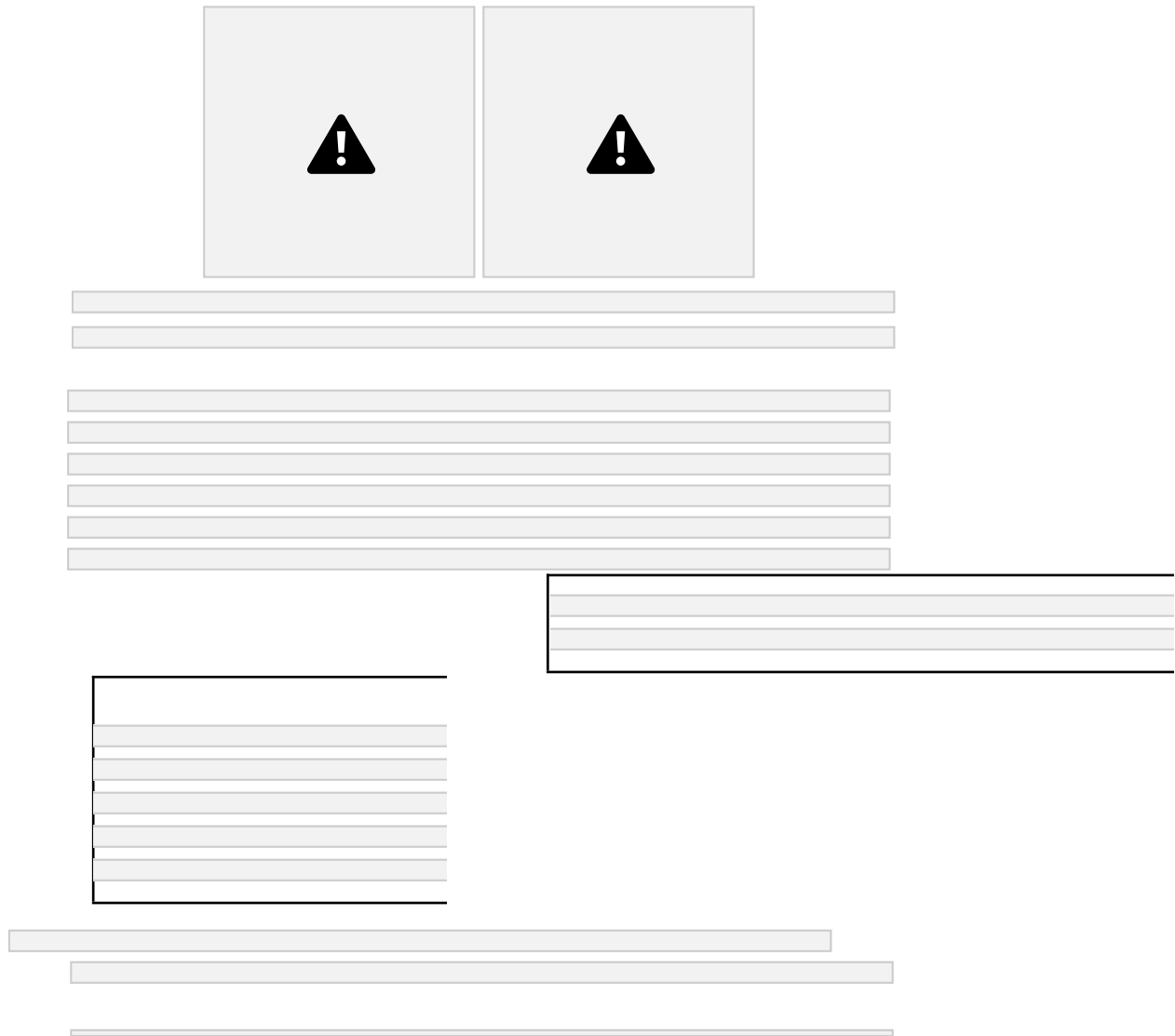
Figure 2.9. With the lumen boundaries automatically segmented in all frames, the entire pullback can be 3-D rendered with a plot of the lumen area at each position side-by-side. In this example, the calculated MLA is in region B. In comparison, region A also has small lumen areas (but larger than MLA), and may be disregarded if only single frame numbers are observed. However, region A is proximal to region B, and might be hemodynamically more significant than region B (expected distal vessel tapering).

Assuming the image data have been already log compressed and read into the memory, the running time of the entire method written in mixed MATLAB and C programming languages is about 15s for segmenting 180 frames in a pullback on a duo core 3 GHz computer. This is fast enough to be considered for real-time clinical use.

2.6 Discussions

The main contribution of this study is the development of a 3-D optimal method for fast lumen segmentation in IVOCT. We proved that, even without any manual correction, the proposed method can more accurately determine the MLA than human analysts from the whole pullback. In addition to MLA, the proposed method is also accurate for segmenting general IVOCT images.

A key advantage of our method over previous methods (67, 70-73) is its 3-D optimal nature. None of the previous studies can guarantee the globally optimal lumen boundaries for the whole pullback. Because of this, the method is extremely robust and is able to handle images with different quality and various artifacts. This is ideal for clinical use. Compared to one of the state-of-the-art method employed in the commercial software, our method is significantly more accurate in segmenting lumen boundaries. From a practical perspective, our method will effectively reduce the manual correction time significantly, and facilitate real-time applications during the clinical procedure.

Another contribution to the robustness lies in that there are very few heuristics involved in the method, whereas most previous methods used some form of heuristics (e.g. thresholding) for lumen segmentation. Importantly, by formalizing the processing in a multi-resolution scheme, the 3-D optimal lumen boundaries can be efficiently computed in tens of seconds. With faster sweeping light sources and data acquisition devices in the future, the number of A-lines and the number of pixels/A-line may be further increased. In such cases, we can always downsample the high resolution images to the coarse level used in the current study, and compute the optimal lumen boundaries efficiently using the

two-round multi-resolution segmentation technique. Therefore, the proposed method is

fully compatible with future generations of IVOCT systems and has a great potential for real-time clinical usage.

The proposed method is operated in polar coordinates and assumes the lumen border intersects each A-line exactly once. A limitation associated with this assumption is that the method may fail in segmenting concave lumen borders. Fig. 2.10 shows an example of such cases where there is a large discontinuity at 9 o'clock possibly due to motion artifacts. The smoothness constraint between adjacent A-lines prevents the contour from reaching the true lumen boundary. However, such cases only constitute a small portion of real-world clinical images and in most situations the smoothed contour given by the algorithm can be accepted according to the consensus of analysts participated in this study.
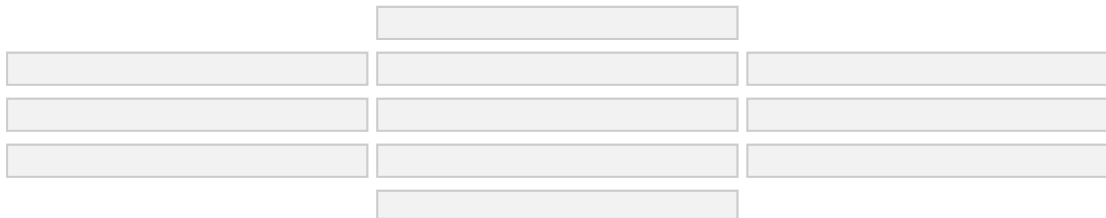
Figure 2.10. An example where the algorithm failed to correctly segment the lumen boundary at 9 o'clock (arrow).

The clinical implications of our work are numerous. As seen from this study, although the lumen border is much more distinctive in IVOCT than in IVUS, there is still significant inter-observer and intra-observer variability in assessing MLA and vessel diameters. The automated method can eliminate this variability and make the measurement more consistent. The choice of device sizes used during PCI, notably stents

and balloons, relies fundamentally on lumen dimensions which can be now obtained in a rapid and reliable method, allowing shorter procedural time. The algorithm can also be used for offline analysis of images in clinical trials, reducing the analysis time of a single pullback from hours down to tens of seconds. Moreover, as shown in Fig. 2.7, the 3-D lumen segmentation method allows extracting the 3-D volumetric profile of the vessel in short time, thereby providing more comprehensive and detailed morphological information than single-frame numbers. This could serve as a valuable intra-operative tool for guiding real-time interventional strategies and procedures. Furthermore, robust lumen segmentation is a fundamental step in any atherosclerotic plaque and stent analysis. For example, the determination of the depth of coronary calcification (96), volumetric quantification of the cap thickness in thin cap fibroatheromatous plaques (67), automated stent strut detection and quantification of malapposition and neointima area (77, 97) all rely first on an accurate lumen tracing.

Chapter 3. Computer-aided 3-D Quantification of Fibrous Caps (FC)

3.1 Motivation

Most acute coronary events result from rupture of the protective fibrous cap (FC) overlying an atherosclerotic plaque (98). Thin cap fibroatheroma (TCFA) has been identified as the most frequent precursor lesion that leads to plaque rupture (7). TCFA has been characterized as a plaque containing a large lipid necrotic core covered by a thin FC infiltrated by macrophages (7, 9). An *ex vivo* morphometric assessment of 41 ruptured coronary plaques revealed that the mean cap thickness was 23 ± 19 μm and 95% of these FCs measured less than 64 μm (99). Because of this, a thickness of 65μm has been considered the instability threshold, and thickness of the FC has been considered one of the major morphometric determinants of those plaques prone to rupture (7, 9). IVOCT is currently the only imaging modality that can measure the FC thickness *in vivo* (100).

OCT has already been used in several *in-vivo* studies to assess the correlation between the incidence of TCFA/FC thickness and clinical presentations in living patients (101-108).

The current accepted standard method for assessing FC thickness using OCT images is based on single measurements of the thinnest portion of the FC (100, 109). In practice, the segment of interest of the coronary vessel is imaged in 3D using a catheter probe and a pull-back procedure. The image data are subsequently analyzed manually by expert analysts. The cross-sectional image within a field of view encompassing a lipid-rich plaque where the FC thickness appears to be thinnest is visually identified. The OCT criteria for identification of a lipid-rich plaque are the presence of a signal-poor region with diffuse boundaries and high attenuation (34). In the selected cross section, the thinnest portion of the FC is visually determined and its thickness is manually measured.

55

In order to decrease variability, averaging multiple FC thickness measurements has been proposed (104, 110).

However, there are two limitations associated with this method. First, the measured FC thickness is subject to inter-observer variability due to visual uncertainties involved in the entire process. Second, the FC is intrinsically a 3-D structure and single point/-single frame measurements are unable to characterize the volumetric nature of FC. Although the thickness of FC has been suggested a risk factor for plaque rupture, the exact mechanisms behind FC thinning and plaque rupture are unknown. A more consistent and comprehensive method for FC quantification may better elucidate the unknown factors associated with plaque rupture. In this study, we present a new, computer-aided algorithm for semi-automatic volumetric quantification of the FC (67). With this method, the circumferential distribution of the lipid plaques/FC was first identified by human analysts

in all frames containing FC, then the FC boundaries in the radial dimensions were automatically segmented and volumetric quantification was performed on the segmented FC.

3.2 Method

The OCT raw data were logarithmically compressed and transformed from the polar coordinates (θ, r) to the Cartesian coordinates (x, y) consisting of 1024 by 1024 pixels (pixel size: 9.4 by 9.4 μm). The major steps for volumetric quantification of FC are (1) segmentation of FC boundaries in all frames containing the lesion, and (2) quantification based on the segmentation.

3.2.1 Segmentation of FC Boundaries

FC is delineated by a luminal boundary and an abluminal boundary. In the non ruptured plaque the FC protects the underlying lipid/necrotic core from contacting the circulating blood. Therefore, the luminal boundary coincides with the vessel lumen contour. The abluminal boundary is commonly described as the "diffuse border" created by the interface between the FC and the underlying lipid pool. We assume the lumen contour has been already detected using the method described in Chapter 2. We next focus on segmentation of FC abluminal boundaries.

The FC abluminal boundary is the optimal boundary that best separates the FC from the underlying lipid plaque. Therefore, by designing an appropriate cost function, we can use dynamic programming (Section 2.1.1) to extract this optimal boundary. Although OCT has been suggested to have the ability to quantify FC thickness accurately (109), a

quantitative definition of the FC abluminal boundary under OCT has not been proposed. The FC abluminal boundary is usually characterized by a gradual transition of pixel intensity from bright to dark, and visual determination of the optimal transition point can be cumbersome, inaccurate and subject to high variability. On the other hand, given an objective function favoring the appropriate properties of FC, computers can objectively identify the location of the abluminal boundary more consistently than humans. The FC has been defined histologically as a distinct layer of connective tissue covering the lipid core, and consists purely of smooth muscle cells in a collagenous-proteoglycan matrix, with varying degrees of infiltration by macrophages and lymphocytes (9). The fibrous tissue appears bright by OCT and has a low attenuation coefficient, whereas the lipid pool appears dark and strongly attenuates the light (78, 79). Therefore, we suggest that

57

the FC abluminal boundary has a high intensity difference between the FC and lipid pool, and also a high gradient. Hence, we define the following objective function:

$$\max \_ (,) (,) (,) \, _{l \, \alpha \, \alpha} f FC \, i j \, I \, i j \, d \, j j \, I \, i j j \, d = - \leq \leq - \, < \, \leq \, - \, \lambda \mu \, (7)$$

Where $_l d$ and $_{max} d$ are predefined depths to calculate pixel intensity difference, μ is the slope of pixel value attenuation extracted from the A line segment of length L across (i,j), and λ is a weighting term. The parameter values $75 \, _l d = \mu$m, $_{max} d = 0.38$ mm, $\lambda = 7$ and $L = 38 \, \mu$m used in the validation set were determined experimentally using a separate training data set (n=3) different from the 14 lesions selected for validation. The ROI for analysis is bounded in the radial dimension by the previously segmented lumen boundary and a predefined maximum depth $_{max} d$, and in the circumferential dimension by a user-defined starting and ending angle encompassing the selected lesion.

3.2.2 Volumetric Quantification

With the fully segmented FC, we can quantify the thickness at each point of the FC luminal boundary, defined as the minimum distance from this point to the FC abluminal boundary. The conventional metric, the *minimum FC thickness (MCT)*, of a single lesion can be simply found by searching for the minimum thickness out of all the points on the FC luminal boundary in all consecutive frames covering this lesion. The *mean FC thickness (MeanCT)* of a lesion is the average thickness of all points on the FC luminal boundary.

In addition, volumetric metrics of the FC can be defined as follows. The *FC surface area (SA)* of a lesion can be calculated as the product of the frame interval and the arc length of FC summed over involved frames. The arc length can be determined from the

radius of FC luminal boundary with reference to the centroid of the lumen. The *absolute* and *fractional FC categorical surface area (ACSA and FCSA)* of a lesion can be calculated as the absolute and relative FC area in a thickness category. In this study, we classified FC thickness into 3 categories: <65μm, 65-150μm and >150μm. This definition is based on both pathology studies and *in vivo* clinical studies using OCT (9, 108). However, further evaluation of the significance of these cut-off values will be important in the future. *FC volume (Vol)* of a lesion is calculated from cross sectional FC areas in individual frames using Simpson's rule. *FC volume density (VD)* of a lesion is the FC volume normalized by the lesion length. *FC fractional luminal area (FLA)* is defined as the percentage of luminal area occupied by the FC. *Categorical FC fractional luminal area (CFLA)* is defined in a similar way but only counting the FC area in a thickness

category. Cross correlation between the volumetric metrics will be used to evaluate redundancy (collinearity).

3.3 Experimental Studies

Three experienced OCT analysts were involved in the validation experiments. A graphical user interface written in MATLAB (MathWorks, Inc) and C++ for visualizing and analyzing OCT images was developed and provided to the analysts. Importantly, proper calibration of all OCT image runs through adjustment of the Z-offset was performed by a single operator, and kept the same by the other two analysts and by the computer algorithm. Likewise, the same operator was responsible for selecting all lipid rich lesions included in the analysis.

In order to allow a comprehensive understanding of the importance of a full volumetric segmentation of the FC, inter-observer variability of FC thickness

quantification of all 14 lesions were initially determined by the single-frame, single measurement concept among the three analysts. In this process, each analyst independently selected the image frame where they suspected the FC was thinnest and determined the FC thickness by a single measurement.

Subsequently, all 323 cross-sectional images from the same 14 lipid-rich lesions were manually segmented by analyst 1 and by the computer algorithm. The accuracy of the computer algorithm was evaluated by comparison with the manual segmentation. In order to assess intra-observer variability, all images were re-analyzed by operator 1 two weeks later. To assess inter-observer variability of manual segmentation of FC boundaries, 50 randomly selected cross-sections were analyzed by operators 2 and 3. At all times, each

analyst was blinded to the analysis results performed by the other analysts and the computer algorithm. Only the common region of FC selected by all three analysts was used for comparison. If the FC was blocked by the guide wire shadow, only the shadowed region was excluded for validation.

Since the algorithm determines both the luminal and abluminal boundaries of FC, we evaluated the accuracy of every point on the two boundaries as illustrated in Fig. 3.1. If we project n rays from the lumen centroid to the FC at one degree intervals, and define the distance from the lumen centroid to the FC luminal and abluminal boundary along ray i as $\_{i}d\,LB$ and $\_{i}d\,ALB$, respectively, we can use the mean absolute difference (MAD) between these distances determined from the semi-automatic method and manual segmentation to assess the agreement:

$$MAD\,d\,LB\,d\,LB\quad MAD\,d\,ALB\,d\,ALB \qquad (8)$$

60

The mean signed differences (MSD) can be similarly defined. This stringent metric allows complete comparison of every point on the FC boundary.
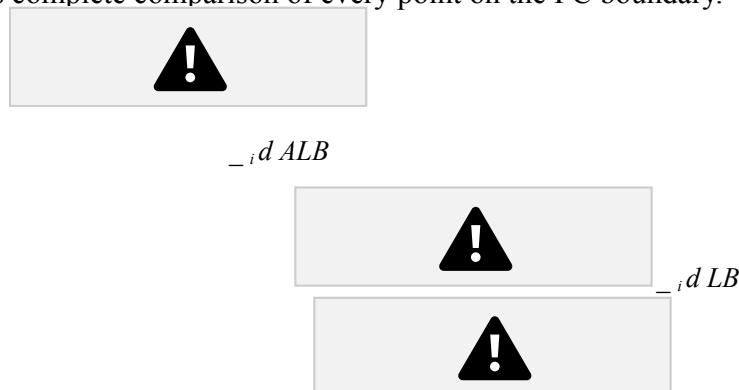

$\_{i}d\,ALB$

$\_{i}d\,LB$

Fig. 3.1. Methodology for validation of fibrous cap luminal and abluminal boundary determination. The

distance from the two boundaries to the lumen centroid was defined as $\_{i}d_{LB}$ and $\_{i}d_{ALB}$, respectively, and compared between the computer algorithm and human analysts. This distance was calculated along rays at intervals of one degree.

3.4 Results

The intra-observer variability in determining the minimum cap thickness (MCT) was 14.5±11.7μm for analyst 1. Figure 3.2 illustrates the manually measured MCT by the three analysts. The concordance correlation coefficient (CCC) of the frame selection was excellent (ccc=0.9958) among the three analysts, with a mean absolute difference of the selected frame for assessing the MCT of 3.1 ± 4.1 frames. However, the mean absolute difference between the three analysts in assessing the MCT of the 14 lesions was 12.8±8.2 μm, with a very poor CCC (ccc=0.2450). Of note, when the cut-off point of 65 μm was used to define a TCFA, agreement among all three analysts was reached in only four lesions and at least one analyst held a different assessment in 10 out of the 14 lesions.
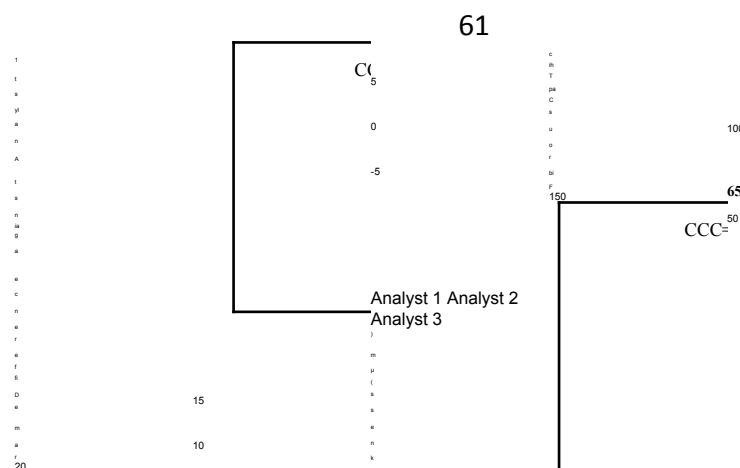
61

Fig. 3.2. Manual measurements of the minimum cap thickness of the 14 lesions by the three analysts. (a): The difference of the selected frame for measuring the minimum cap thickness by the three analysts was plotted vs. the lesion number. The frame difference is against analyst 1. Frame difference of 0 indicates no difference. (b): The minimum cap thickness measured on the selected frame in (a). CCC: concordance correlation coefficient. CCC<0.4 is considered to be poor agreement. Dashed line: conventional cut-off value of 65μm for definition of TCFA. Under this definition, one of the three analysts held a different assessment of TCFA for 10 out of 14 lesions.

The Mean Absolute Difference (MAD) of the segmentation performed by human analyst 1 in two different time points was 20.7±11.3μm. The MAD between the three human analysts was 30.3±27.3 μm. The angular difference of the selected circumferential distribution of FC for the three analysts was 9.6±9.9 degrees for all lesions except for one outlier (63.0 degrees).

The average processing time for lumen segmentation, guide wire segmentation and FC abluminal boundary determination in a single frame was 0.4s, 0.07s and 0.2-0.4s, respectively (with a duo core 2.00GHz CPU).

The MAD of the FC thickness between the algorithm and analyst 1 in assessing all the 323 images was 27.3 ± 26.7μm. The MAD of the luminal and abluminal boundary was 15.7 ± 23.4μm and 25.3 ± 31.4μm, respectively. The Mean Signed Difference (MSD) of the FC thickness, luminal and abluminal boundary between the algorithm and analyst 1 was 2.9 ± 38.0μm, 6.0 ± 27.5μm and -3.2 ± 40.2μm, respectively.

Figure 3.3 shows the MAD and MSD comparison of the localization of the luminal and abluminal boundaries and the thickness of the FC by the algorithm and by the three

62

analysts. The MAD between the algorithm and analysts was comparable to that between analysts. The MAD for luminal boundary was less than that for the abluminal boundary.

From the MSD results in Fig. 3.3 (b), the bias is around one pixel or less, except between analyst 3 and the algorithm and between analyst 3 and the other two analysts in determining the FC abluminal boundary (and consequently the FC thickness).

FC thickness FC luminal boundary FC abluminal boundary

(a)

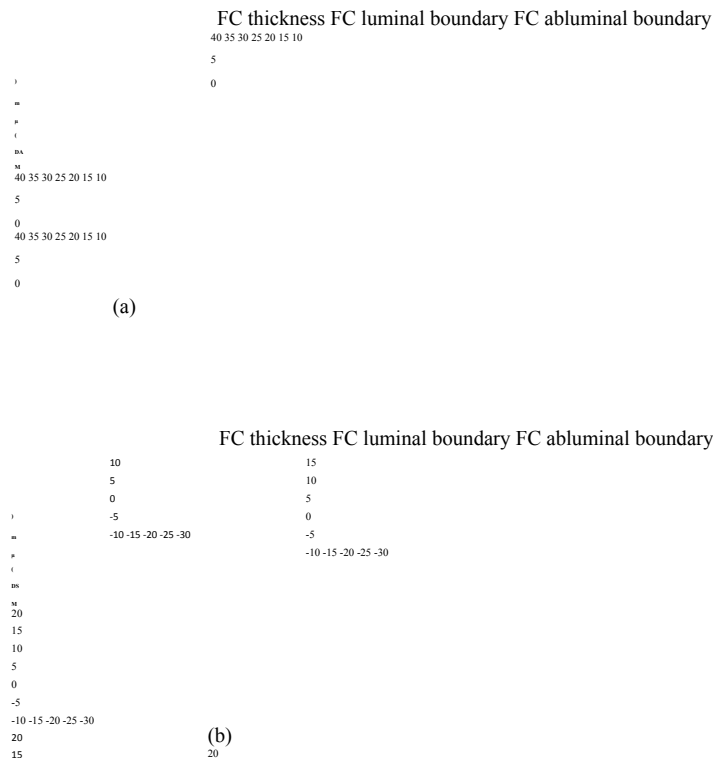FC thickness FC luminal boundary FC abluminal boundary

(b)

Fig. 3.3. (a): Mean absolute difference (MAD) between automated and manual measurements by three observers. (b): Mean signed difference (MSD). Left: fibrous cap thickness determination. Middle: Luminal boundary determination. Right: Abluminal boundary determination. O: observer. Auto: computer algorithm.

Figure 3.4 illustrates a typical example where the semi-automatically determined contour was very similar to all three analysts. While the analysts tended to smooth the FC boundary, the algorithm exactly followed the border where the intensity difference and gradient were high. Figure 3.5 shows an example where the algorithm shows disagreement with the three analysts. Compared to the algorithm determined segmentation, the FC traced by analyst 2 is significantly thinner, whereas the one traced

by analyst 3 around 9-10 o'clock is thicker.

Figure 3.4. In this case, the semi-automatically segmented fibrous cap boundary showed good agreement with all three human analysts.
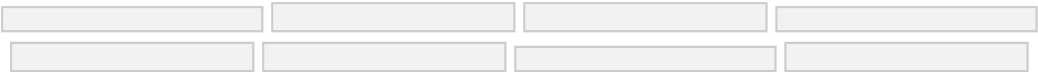
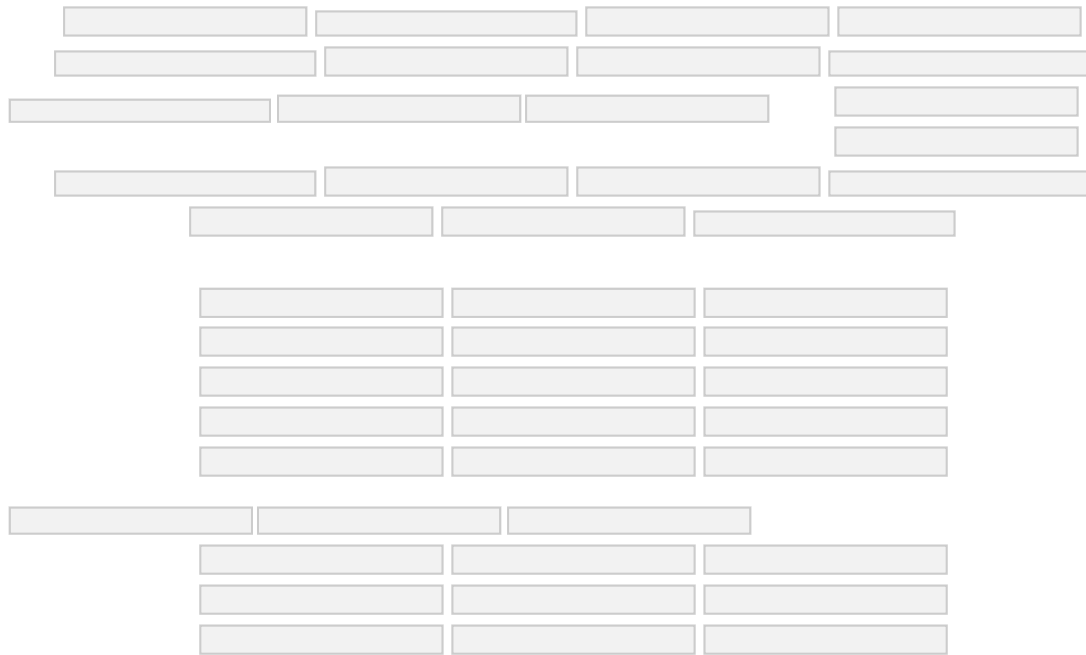Fig. 3.5. In this case, the algorithm shows disagreement with the 3 analysts. The traced FC from analyst 2 is significantly thinner than that from the algorithm. In comparison, the FC traced by analyst 3 around 9-10 o'clock is significantly thicker. Analyst 1 selected more circumferential distribution of FC for segmentation.

Among the 14 lesions, there was low correlation between all the volumetric metrics and the conventional metric MCT (Table 3.1). This indicates that these volumetric

64

metrics characterize independent morphological information about FC. Between the volumetric metrics, there was moderate correlation between ACSA (<65μm) and MeanCT (R=-0.67, p<0.01), between FCSA (<65μm) and MeanCT (R=-0.76, p<0.01), between CFLA (<65μm) and MeanCT (R=-0.65, p<0.01), between ACSA (<65μm) and SA(R=0.74, p<0.01), between ACSA (<65μm) and Vol (R=0.64, p<0.01), between FLA (<65μm) and SA (R=0.64, p<0.01), between VD and SA (R=0.77, p<0.01), between VD and FLA (R=0.77, p<0.001), and between VD and Vol (R=0.82, p<0.001). There was strong correlation between Vol and SA (r=0.99, p<0.0001).

The segmented FC can be visualized in 3D with a continuous colormap, from blue to green to red, indicating the FC thickness ranging from 300µm to one pixel length. Figure 3.6 illustrates 2 cases, both with TCFA, with FC thickness rendered in 3D. If assessed using only the conventional methodology, the morphological differences between the cases would not be apparent. However, the 3-D visualization demonstrates dramatically different characteristics. In particular, the vessel shown in the lower panel has a significantly higher fraction of thin FC as compared to the one in the upper panel.

Table 3.1. Correlation coefficients between the volumetric metrics in 14 lesions

	MCT	MeanCT	FCSA	ACSA	FCSA (<65µm)	ACSA (<65µm)	SA	FLA	CFLA		Vol	MCT	MeanCT	FCSA	ACSA (<65µm)	Vol
VD	0.02	0.18	0.35	-0.49	0.77*	0.77**	-0.26	0.82**		Vol	-0.31	-0.14	0.64*	-0.30	0.99***	0.63	0.08
CFLA (<65µm)	-0.23	-0.65*	0.39	0.47	0.17	0.11										
FLA	0.04	-0.11	0.45	-0.28	0.64*											
SA	-0.37	-0.27	0.74*	-0.19												
FCSA (<65µm)	-0.20	-0.76*	0.44													
ACSA (<65µm)	-0.49	-0.67*														
MeanCT	0.34															

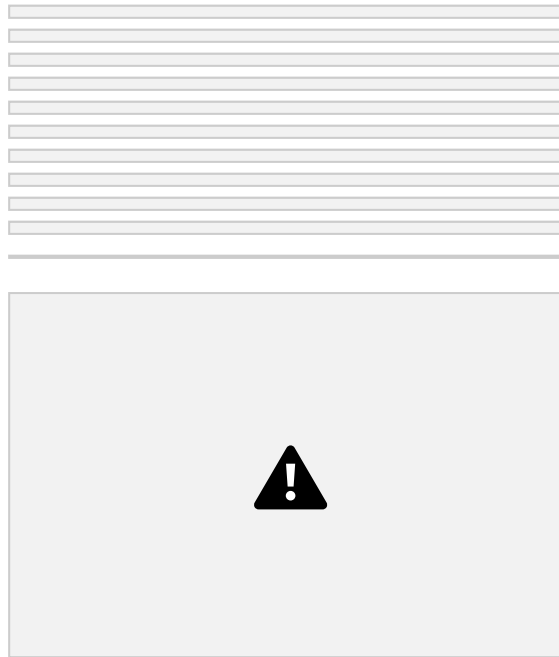Significance levels: *p<0.01, **p<0.001, ***p<0.0001.

Fig. 3.6. Two coronary arteries used in the validation study with fibrous caps (FC) rendered in a continuous color map indicating the thickness. Both of the two lesions contain TCFA (red arrows) and similar minimum cap thickness. However, the one shown in the lower panel contains a significantly larger surface area with thin cap as compared to the one in the upper panel.

3.5 Discussions

A fibrous cap (FC) with the minimum cap thickness< 65µm has been used as the threshold to characterize TCFA by histopathology (9), but no causal relationship can be derived for prediction of plaque rupture. While largely accepted, the determination of this value may be affected by artifacts from histology preparation such as tissue shrinkage, and selection bias (this cut-off was derived from plaques that had already ruptured). A recent OCT study on 266 lesions suggested that 80 µm might be the critical cap thickness that may confer instability to a coronary plaque in living patients (108). However, OCT and pathology studies were based on single or multiple individual FC measurements and significant variations can be expected, as shown in the present study (Fig. 3.2). The

MAD of 12.8±8.2 µm among the three analysts was actually below the resolution of the

OCT system. However, the reported incidence of TCFA can differ dramatically if 65μm was chosen as the single threshold (Fig. 3.2 (b)). One particular challenge for human analysts is to identify the particular frame containing the cap with the minimum thickness. In this study, while the three analysts chose the same frame for most of the lesions, the difference in selection of the site to measure the minimum FC thickness could be substantial for some lesions (e.g. lesion 2 in Fig. 3.2(a)). The computer-aided method tested in this study provides semi-automatic segmentation of the whole FC, which eliminates the uncertainty associated with manual analysis and image selection and allows more accurate determination of the true minimum FC thickness.

Xu et al (78) has found that lipid plaques have higher backscattering coefficient as compared to FC. Therefore, the study suggested that the true FC boundary is actually within the signal-rich region. If this is true, the FC boundary may precede the steepest decline, and both human analysts and our method may overestimate the FC thickness slightly. However, direct search for the true boundary as a local peak may not be straightforward for human analysts or for algorithms. In clinical images, such peaks are not always present, and even when present, are not readily discernable from surrounding speckle noises. In addition, the presence of macrophages can also cause very strong peak signals. In comparison, searching the maximum gradient and intensity difference to represent the boundary is relatively robust and consistent, which is more important clinically than a slight bias. We will perform further validation studies to confirm the true FC location. As tissue shrinkage and the difficulty for precise registration associated with histology may make it difficult for such validation, a volumetric validation method using

Cryo-imaging (111, 112) that gives better registration may be used. If appropriate, an offset value may be added in the model to compensate for the bias.

A fundamental limitation of the single number description of the FC thickness is the lack of appreciation for the 3-D morphology of FC. While the mechanisms associated with FC rupture remain elusive, it is possible that mechanical stability of the cap may not only depend on the focal point thickness, but also on the thickness of non-focal regions. Moreover, plaque rupture may not necessarily happen at the thinnest part of the FC. These unknown morphological and mechanical properties that ultimately lead to plaque rupture can now be investigated in future studies with the help of the volumetric quantitative method.

Among the volumetric metrics, the *FC surface area* in a certain thickness category reveals the component of the FC in a certain thickness range. One may speculate that a FC with a larger area of thickness<65µm may be more vulnerable than a FC with a smaller area of thickness<65µm. The *total and categorical FC fractional luminal area* is more precise than using the number of quadrants to represent the distribution of lipid-rich plaques. The *FC volume* is strongly correlated with the *FC surface area*. This is not surprising because both metrics depends more on the lesion length rather than the lesion thickness due to the large frame interval (200µm) of the current OCT system. We could speculate that vulnerability increases with surface area and decreases with thickness, so volume may be less sensitive than surface area even though it includes more information.

Figure. 3.7. In this case, the computer algorithm mistakenly identified luminal blood as part of the tissue due to the contact between the blood and lumen boundary. In the blood-free region, the algorithm accurately segmented the boundary as compared to human analysts.

The semi-automatic method is as accurate as expert analysts (Fig. 3.3). It is highly

robust (global optimal nature of dynamic programming) and fast enough (<1s for single frame) to be used in practice.

One limitation of the semi-automatic method is the inaccurate segmentation of the luminal boundary in presence of luminal blood (Fig. 3.7). In this study, only one lesion had residual luminal blood. For validation purposes, no manual correction was performed in this study. However, in practice, users could make necessary corrections in such cases.

The current method is semi-automatic because the circumferential boundaries of a FC were defined manually by the analysts. Automated detection of the circumferential boundaries is challenging because validated (or at least reproducible) criteria for the FC circumferential boundaries in OCT images have not been defined.

The metrics provided in this study only characterize the morphology of the FC. However, the vulnerability of the FC also depends on inflammation (macrophages)

69

within the FC (36) and other factors in addition to FC thickness. For example, Ohayon et al (113) has demonstrated that plaque instability is affected by a combination of cap thickness, necrotic core thickness and the arterial remodeling index. The direction of blood flow towards the FC may also affect the vulnerability (102). Microcalcification within the thin fibrous cap has also been suggested to cause stress-induced plaque rupture (114).

The material in this chapter was published in Biomedical Optics Express and is made available as an electronic reprint with the permission of OSA. The paper can be found at the following URL on the OSA website:

70
Chapter 4. Automated Segmentation and Quantification of Calcified Plaques

Coronary Calcified Plaque (CP) is an important marker of atherosclerosis, and can provide an estimate of total coronary plaque burden for a patient (10-15). Although no clear relationship between calcification and plaque vulnerability has been established (13), an automatic method to segment and quantify CP in medical images would facilitate our understanding of its role in the clinical coronary heart disease (CHD) risk assessment (10). Moreover, heavily calcified lesions are often associated with a lower success rate of coronary stenting and require usage of additional devices like rotational atherectomy (16). Quantification of calcified lesions, such as their depth and thickness, can provide

valuable information for guiding complex interventional strategies in vessels with superficial calcification.

4.1 Level-set Segmentation Method

Level-set is a popular method used for image segmentation (115-117). It tracks the object boundaries by minimizing an appropriately designed energy function on a continuous grid using partial differential equations. Instead of explicitly representing the evolving contours using parametric models like snakes (118), level-set implicitly represents a contour using the zero level set of a higher dimension function, and can treat topological changes such as contour break and merge easily. We define φ(t,x,y) (to simplify description, we use 2-D grid, but level set can be easily generalized to higher dimensions) as the level set function in a higher dimension, and the zero level set $C\,xy$ = = $\{(\ ,\ )\,|\,0\}\ \varphi$ represents the evolving contour. Image segmentation using level sets

71

begins with an initial contour, and then evolves it in the normal direction based on the following general equation:

$$\frac{\partial \varphi}{\partial t} \qquad (9)$$

Where F is a speed function and is related to the image data.

For CP segmentation, we developed a level set approach combining the work of Li et al. (119) and Chan and Vese (120). We define φ as a signed distance function (SDF) with its

zero level curve represented by C . φ <0 if φ is outside C ; φ > 0 if φ is inside C . The initial contour C_0 is driven to the desired CP boundary by minimizing the following energy term:

$$
E = \mu \blacksquare \left[\frac{1}{2} \blacksquare^2 \blacksquare \right] '() + \blacksquare xdy + \upsilon - \iiint_{\Omega\Omega\Omega} \blacksquare \varphi \ g \ H \ dxdy \ 2
$$

$$
+ \blacksquare \left(\ \right)^{22} - \int\int \blacksquare \ \varphi \ (10) \quad {}_{01\ 02} \ \kappa \ \blacksquare \ (1\ ()) \ \blacksquare \ H
$$

$$
dxdy \ _{\Omega\ \Omega}
$$

$\delta(\ )\ \varphi$ is a 2D smoothed Dirac function; H is the Heaviside function; ${}_0 I$ is the original image; $g\ g\ '\ 1/\ (1\ ) = +$, where g is the gradient image which is determined by convolving the original image with different orientations of edge filters and selecting the maximum response for each point (96). ${}_1 c$ is the average intensity inside C and ${}_2 c$ is the average intensity of an outer ring of thickness w surrounding C , μ , λ , υ and κ are weighting terms. The first term is to keep φ as a SDF. The second term is a length term regulating the smoothness of the contour. The third term is an area term indicating whether the curve will grow or shrink. In our implementation, it was set positive to shrink

72

the contour. The fourth term contains region-based intensity information. The minimization of E is based on the following gradient flow:

$$
\frac{\partial \varphi}{\partial t} = -\frac{\partial E}{\partial \varphi}
$$

$$\varphi \ (11)$$

The evolving contour was stopped if it its speed was close to zero. In the discrete image space, all the terms in the above equations are numerically approximated. The level set method requires an initial contour surrounding the CP. The initial contour was generated from binary edge detection followed by morphological dilation. Specifically, A special matched filter (121) was designed to detect the CP boundary (Fig. 4.1(a)). The edge detection was performed in a sequential approach. First, the strong leading edge of CP in the polar coordinate was detected by the filter rotating from -15º to 15º by a 5º interval (angles were with reference to the incident light), and the maximum response at each pixel was set as the final gradient value for that pixel, thereby generating a gradient image. A binary edge mask was obtained by hysteresis thresholding (122) . A horizontal Prewitt operator was then used to fix any possibly missed extremely shallow leading edge with depth smaller than the size of the matched filter. The gradient image for the abluminal edge of CP was obtained following the same procedure but by the filter oriented along different directions. The corresponding binary edge image was generated such that only the edges connected to or were behind the leading edge were included. The final gradient image and binary edge image were obtained by combining the individual responses from luminal edge and abluminal edge together (Fig. 4.1(b)).

Figure 4.1 (a) The matched filter used for edge detection. (b) Binary edge detection result. (c) The initial contour generated from the binary edge image by morphological dilation.

More details of the method can be found in (96). The advantage of the level-set methods is its flexible topology for contour merge and break. The limitation is that it may find a local minimum instead of a global minimum. Therefore, the initial contour is often required to be placed close to the desired boundaries. More details about level sets can be found in (115-117, 123).

4.2 3-D Segmentation Using Graph-cut

In this section, we present a 3-D method for CP segmentation based on interactive graph cuts (93, 94, 124), with the following features, that overcomes the aforementioned limitations. First, graph-cut can be applied to high-dimensional (e.g. 3-D and 4-D) image space easily. Therefore, in IVOCT image stack, it can segment slices with incomplete contour using information from neighboring slices. Second, graph-cut is a global optimization method, which is robust in presence of noises and artifacts. Finally, graph cut allows fast-editing, and can quickly recalculate a new segmentation based on an edited initial segmentation—greatly decreasing calculation time if edits are needed.

In this segmentation regime, users first give a foreground (CP) and background (anything other than CP) input on some slices within the volume to be segmented. In the current implementation, users use a brush to roughly mark the input pixels in every 10 frames. Then, a graph is constructed with 8-neighbourhood system (6 neighbors in the same frame and 2 neighbors from adjacent frames), with each pixel represented by one node. We also add two special nodes, source and sink, representing the foreground and the background, respectively, to the graph. There are two types of edges defined in the graph. N-links are the edges connecting neighboring nodes, and T-links are the edges connected to the source and sink.

The flexibility of the graph data structure further allows us to add additional edges to more realistically represent the helical scanning manner in which the data were acquired. In a given slice n, we add additional N-links from the nodes corresponding to the bottom of slice n with the nodes corresponding to the top of the slice n+1. This provides a natural continuity between frames, and more realistically represents the physical acquisition of the intravascular OCT image. The edges between neighboring nodes in cross-sectional frames are assigned edge weights in proportional to the responses to a matched edge filter, similarly to the one used in the level set method (Section 4.1). The edge weights between neighboring nodes in longitudinal directions are defined as the likelihood of the nodes belonging to the same categories (i.e. foreground or background) according to the histogram of the user input. Then, standard graph-cut algorithms can be applied to find the minimum cut of the graph, which corresponds to the optimal segmentation of the volumetric image stack. Representative segmentation examples are shown in Fig. 4.4.

4.3 Quantification of Calcified Plaques

Four quantitative measures, the depth, area, thickness and angle fill fraction (AFF) can be quantified from the automated segmentation. The calculation of area was trivial. The depth, thickness and AFF were all calculated with reference to the centroid (indicated by O) of the lumen for each individual CP. Fig. 4.2 illustrates the methodology. The depth and thickness are defined as

$$Depth\ D_i = \frac{1}{n}\sum_i^n \qquad Thickness\ T_i = \frac{1}{n}\sum_i^n \quad (12)$$

n is the maximum number of the non-overlap rays radiating from O spanning across the CP. The AFF θ is the largest angle between the spanning rays.
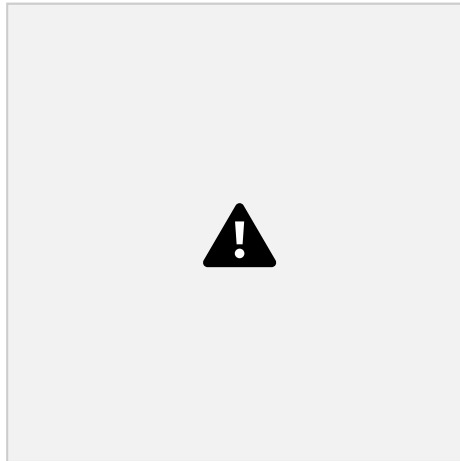

Figure 4.2. Calcified plaque quantification metrics. The yellow dotted lines radiating from the centroid of the lumen serve as the direction along which the depth and thickness are measured. The red and blue double arrows indicate D_i and T_i for depth and thickness measurement, respectively. AFF θ is the largest angle between the rays across the CP boundaries.

4.4 Experimental Studies and Results

We first evaluated the segmentation accuracy of the level-set method. For this study, two independent expert OCT image observers blinded to automatic segmentation results

were involved in the manual contour tracing process, which was performed on commercial OCT workstations. OCT observer 1 finished all 106 images while OCT observer 2 randomly analyzed 63 of the 106 images. The 63 images were used to evaluate inter-observer and computer-observer variability. Automatic and manual segmentation results were compared using Dice coefficient (DSC).

Fig. 4.3 shows three examples of automatic CP segmentation results using the level set method. Fig. 4.3 (a) contains three CPs with clear abluminal edges. Although the CP at 3-4 o'clock is partly blocked by the guide wire, the effect on the auto-manual agreement is negligible. We show in Fig. 4.3 (e) that our method can guess and approximate the part of the CP blocked by the guide wire. A FP region is also shown at 1-2 o'clock. We next demonstrate the performance of the method on a large CP with irregular shape and unclear abluminal edges (Fig. 4.3 (f)). A large disagreement between humans and computer appears on the abluminal edges. The overall DSC for all the CPs is 0.78 ± 0.09. In comparison, the DSC between 2 human observers is 0.89 ± 0.07.

Figure 4.3. Examples of calcified plaque segmentation results. (a–c) Original images. (d–f) Corresponding manual and automatic segmentation results. Red: observer 1; blue: observer 2; yellow: automatic method.

For the 3-D graph-cut method, we demonstrate the segmentation accuracy in Fig. 4.4 (a).

In this example, user provided input on slices 1, 10, 20, 33, and 40. Note how the graph-cut can generate the 3-D segmentation of the CP boundaries in all the slides, even in slices (e.g. slice 24) with incomplete contours. We next demonstrate the "fast-editing" capability of graph-cut in Fig. 4.4 (b). After initial segmentation, user provided a correction input in only slice 27, and all the segmentation in adjacent frames were corrected automatically. Clinical IVOCT images are noisy, and often suffer from various artifacts. In addition, due to the limited penetration depth, many CPs under OCT lack clear abluminal edges. Therefore, we do not expect an image processing method to generate a perfect segmentation. With this fast-editing feature, users can incrementally improve their segmentation efficiently, which is attractive for clinical data analysis. We will conduct more thorough validation studies for the graph-cut method in future studies.

78